

# Geodesic Convolutional Neural Network Characterization of Macro-Porous Latent Thermal Energy Storage

Nithin Mallya<sup>a</sup>, Pierre Baqué<sup>b</sup>, Pierre Yvernay<sup>b</sup>, Andrea Pozzetti<sup>b</sup>, Pascal Fua<sup>c</sup>, Sophia Haussener<sup>a,\*</sup>

<sup>a</sup>Laboratory of Renewable Energy Science and Engineering, Institute of Mechanical Engineering, École Polytechnique Fédérale de Lausanne, Switzerland

<sup>b</sup>Neural Concept SA, Switzerland

<sup>c</sup>CVLab, École Polytechnique Fédérale de Lausanne, Switzerland

---

## Abstract

High-temperature latent heat thermal energy storage with metallic alloy phase change materials (PCMs) utilize the high latent heat and high thermal conductivity to gain a competitive edge over existing sensible and latent storage technologies. Novel macro-porous latent heat storage units can be used to enhance the limiting convective heat transfer between the heat transfer fluid and the PCM to attain higher power density while maintaining high energy density. 3D monolithic percolating macro-porous latent heat storage unit cells with random and ordered sub-structure topology were created using synthetic tomography data. Full 3D thermal CFD simulations with phase change modeling was performed on 1000+ such structures using effective heat capacity method and temperature and phase dependent thermophysical properties. Design parameters, including transient thermal and flow characteristics, phase change time and pressure drop, were extracted as output scalars from the simulated charging process. As such structures cannot be parametrized meaningfully, a mesh-based Geodesic Convolutional Neural Network (GCNN) designed to perform direct convolutions on the surface and volume meshes of the macro-porous structures was trained to predict the output scalars along with pressure, temperature, velocity distributions in the volume, and surface distributions of heat flux and shear stress. An Artificial Neural Network (ANN) using macroscopic properties - porosity, surface area and two-point surface-void correlation functions - of the structures as inputs was used as a standard regressor for comparison. The GCNN exhibited high prediction accuracy of the scalars, outperforming the ANN and linear/exponential fits, owing to the disentangling property of GCNNs where predictions were improved by the introduction of correlated surface and volume fields. The trained GCNN behaves as a coupled CFD-heat transfer emulator predicting the volumetric distribution of temperature, pressure, velocity fields, and heat flux and shear stress distributions at the PCM-HTF interface. This deep learning based methodology offers a unique, generalized, and computationally competitive way to quickly predict phase change behavior of high power density macro-porous structures in a few seconds and has the potential to optimize the percolating macro-porous unit cells to application specific requirements.

**Keywords:** High-Temperature Latent Heat Storage, Phase Change Material, Macro-Porous Structure, Porous Media, Porous Media Pore-Engineering, Heat Transfer, Computational Fluid Dynamics, Geodesic Convolutional Neural Network, Deep Learning

---

## 1. Introduction

Innovative energy storage technologies are necessary for effective and efficient utilization of existing energy sources and its integration with renewable energy sources. With over 50% end energy usage being heat [1], thermal energy storage is essential in this transformation with high-temperature industrial heat being particularly interesting targets. Latent heat storage utilizes the isothermal solid-liquid phase change process to store thermal energy where charging and discharging of a latent heat storage is performed using the flow of a heat transfer fluid (HTF) around the Phase Change Materials (PCMs) enclosed within high melting point encapsulated structures. High energy and power density applications are achievable in high-temperature latent heat storage by replacing the commonly used molten salts and organic acid PCMs with metals or alloys [2, 3, 4, 5] that

have two orders of magnitude larger conductivities. The higher thermal conductivities of metals make the convective heat transfer rate from the HTF to the PCM encapsulations the limiting factor for dis/charging rates [6, 4]. Due to the extensive use of tubular heat exchangers and their ease of manufacture, latent heat storage has often (around 70% of the time [7]) been investigated in cylindrical encapsulation geometries. Heat transfer enhancement strategies have centered around creating internal or external fins [8, 9, 10]. While low conductivity PCMs are limited by the conductive heat transfer inside the PCM storage units, high-conductivity PCMs require PCM-HTF convective heat transfer enhancements outside the storage units.

The use of engineered porous structures for heat transfer enhancement either as metal matrix-PCM composites for low-conducting PCMs or as external layers for high-conducting PCMs is well known. Experimental and numerical studies using high porosity (0.88 - 0.96) porous metal matrices with a low-conducting PCM like paraffin [11, 12, 13, 14] or n-eicosane [15] resulted in a 2 to 4 times faster rate of melting and up

---

\*Corresponding author: Tel.: +41 21 693 38 78

Email address: sophia.haussener@epfl.ch (Sophia Haussener)

to 44 times increase in thermal conductivity, with a more uniform temperature distribution throughout the PCM. A numerical study of external metallic porous layers surrounding metal cylinders with air as HTF [16] demonstrated increased heat transfer rate dependent on macroscopic parameters such porosity, permeability, and thermal conductivity of the porous layer, at the expense of a larger pressure drop requiring optimization of the porous media parameters. Higher porosity has been experimentally verified [17] to increase Nusselt numbers i.e., heat transfer rates and decrease pressure drops due to enhanced permeability. However the effect of pore density and other parameters was not explicit with a clear dependency on the Reynolds number in porous media of porosity 0.90-0.94 and pore densities 20-80 PPI. The often ignored pressure drops within such porous media based heat transfer enhancements are of particular importance due to the requirement of high-pressure (and high-temperature with metallic PCMs) pumps which increases the power requirements and cost of a LHTES setup. Convective heat transfer and pressure drop correlations dependent on porosity, cell density, and material have been studied in combined numerical-experimental approaches. However, numerical studies predominantly concentrate on volume-averaged correlations based approaches [18, 19] to obtain pressure drop and heat transfer predictions and ignore the pore-level topology of the porous structures themselves. The studies that focus on realistic depiction of metallic matrix-PCM composites [20, 21, 22] find that the pore-level design of porous media are important to increasing power capacity with increasing surface area or decreasing pore size of the foam matrix. An experimental study of different ceramic porous structure designs [6] reinforces the importance of clogged flows due to design or manufacturing defects leading to unexpected high pressure drops and increased thermal dispersion. The thermo-fluidic performance of a porous media is thus dependent not only on the macroscopic properties but also on the pore-level topology and needs to be designed and optimized based on the application.

A numerical study of enhancing convective heat transfer between high-conducting eutectic Si-Mg alloy PCM encapsulated in cylindrical tubes surrounded by ceramic porous media [23] focused on optimizing the relative geometrical dimensions of the tubes and the porous layer to increase heat transfer rates instead of the macroscopic parameters of the porous media. Larger layers of porous media increased the heat transfer rate but resulted in a larger pressure drop and crucially, the loss of latent heat energy density of the storage. A megajoule scale test-bed demonstration of high-temperature aluminium alloy PCM [5] with the same SiSiC layers setup experimentally demonstrated the importance of porous media in maintaining a steady exhaust temperature of the HTF by increasing HTF-PCM convective heat transfer, but resulting in a large pressure drop and reduced latent heat storage capacity.

Utilization of porous media as heat transfer enhancements reduce the latent heat storage capacity and, thus, energy density of the storage unit. Metallic percolating macro-porous encapsulated PCM structure of application specific optimized shapes are a novel and promising alternative for heat transfer enhancement for high-temperature latent heat storage, especially with

the advent of additive manufacturing for convoluted metals and ceramics parts [24, 25]. In contrast to utilization of porous fins, the energy density of the storage unit is not decreased as the macro-porous heat transfer enhancement incorporates the PCM within itself. High-temperature latent heat energy storage can achieve higher power and energy densities using the novel macro-porous encapsulated structures. However, the specific topology that would maximize heat transfer and energy capacity while minimizing pressure drop is not straight forward to determine. An optimal simulation based strategy would be computationally and memory light for behavior prediction of the macro-porous structures, while being flexible enough to allow for both global sub-structure modifications and local refinements for application based optimization.

Studies on improving heat transfer using porous structures for latent heat storage focus on parametric optimization by manually or heuristically varying geometric properties (encapsulation sizes, fin diameter, fin orientation, aspect ratio of porous fins and porous matrices, etc.) [8, 23, 26, 27, 28], or macroscopic properties of the porous media (porosity, mean pore size, specific surface area, etc.) [21, 22, 29], with most studies ignoring the induced pressure drop. These investigations are based on the preconceived topology configuration assumed by the researcher and parameters chosen by their experience, limiting the set of explored porous structures to a low-dimensional design space. Density-based approaches called adjoint methods where material distribution within a spatial domain is varied based on the gradient of the fitness function subject to design constraints have been applied in heat transfer [30, 31, 32], radiative scattering [33], and in designing the spatial layout of high-conducting fins for cylindrical encapsulations in latent heat storage [34, 35, 36] to decrease phase change times with minimum loss of latent storage volume to fins. These methods are computationally expensive requiring rerunning of the simulation to recompute the fitness function at each iteration of the optimization process. One of the classical approaches to reduce the number of computations relies on Kriging [37, 38] where Gaussian Process regressors are trained to interpolate the fitness function based on a low-dimensional design space parametrization. But these methods need to be redefined depending on the problem and require retraining the regressor for change in parametrization. While simplified optimization techniques are favored for reducing design lead times, development of computationally frugal and comprehensive solutions involving topology structure of the porous media are essential for computational design of percolating macro-porous energy storage systems.

Deep learning methods are well known for learning data representations of varying degrees of complexities and have been used to either improve solution performance or to identify physics. Studies on the former assume the physics required for the modeling and use deep learning methods to accelerate simulations such as replicating Reynolds Averaged Navier-Stokes (RANS) flow modeling [39] or replacing the computationally expensive steps in a Poisson flow solver [40]. Physics-based neural networks [41] that incorporate the explicit constraint of the Navier-Stokes equation in the loss function of the neural

network have also been used for full fluid flow partial differential equation (PDE) modeling in turbulent Rayleigh-Bénard flows [42], quantify flow and heat fields from data measurements [43], and in solid-liquid phase change problems [44]. Physics identification deep learning methods are unsupervised learning techniques used to recognize underlying correlations such as using Convolutional Neural Networks (CNNs) to predict the local heat flux in turbulent channel flows with wall shear stress and pressure as inputs [45], to regress steady state velocity in a 3D domain using only the boundary conditions and object shape [46], with a 292x speedup that increases with batch size.

Artificial Neural Networks (ANNs) have been applied in porous media for autonomous characterization of 3D porous samples [47, 48]. They have been used often for performing feature selection of macroscopic and pore-network properties to optimally characterize permeability of the porous media [49, 50, 51, 52, 53] using 3D images from CT-scans. In thermal applications context, ANNs have been used to predict the oxygen output in a solar-driven porous thermochemical reactors based on their macroscopic properties [54], and to predict radiative properties within 2D opaque and transparent porous media and packed beds [55, 56] to replicate the computationally expensive Monte Carlo ray tracing-based results. The 3D CNN has been used to predict the steady state solution of the Navier-stokes laminar flow equation in a porous structure [57] with macroscopic features (Euclidean distance, maximum inscribed sphere size, and time of flight) and the binary images as inputs. It was shown that the 3D CNN trained with sphere-packed porous structure could predict velocity fields in other synthetic geometries, and in X-ray derived structures of sandstone and carbonate with 75% to 98% accuracy. However, utilization of 3D CNNs for training results in either a coarse space discretization or a large memory footprint making them computationally expensive to train, while also not being an ideal framework for topology optimization.

While porous media can be characterized using macroscopic properties, a unique parametric description cannot be provided which makes exploring this vast high-dimensional domain challenging. Geodesic Convolutional Neural Networks (GCNNs) have been shown to reliably emulate a 3D CFD simulator [58] by directly performing convolutions on the surface and volume meshes of the macro-porous unit-cells. GCNNs are thus well suited for training and optimization of structures that cannot meaningfully be parametrized and thus are outside the purview of manual and heuristic prediction and optimization methods. While training of such GCNNs are typically in the order of tens of hours, predictions are obtained in seconds and application specific structures can be obtained in the matter of a few minutes. Turbulent aerodynamic characteristics of aerofoils and cars have been predicted with 86% accuracy and utilizing a gradient-based optimization on the GCNN to move the vertex positions of the mesh and optimize the aerofoil/car shape [58]. GCNNs are particularly attractive for the characterization of the 3D percolating macro-porous latent heat storage unit cells as the surface and volume mesh vertex positions themselves can be used as parametric descriptors of the structure.

The specific objectives of this study is to utilize deep learning techniques to predict the heat transfer behavior of the percolating macro-porous latent heat storage unit cells, as a first step towards free form optimization. The specific steps followed in this paper to achieve this are:

1. Create a computational framework for generation of realistic percolating macro-porous latent heat storage unit-cells with customized macroscopic properties and random/ordered sub-structures.
2. Perform transient 3D thermal CFD phase change simulations on the macro-porous unit-cells with a high-temperature aluminum alloy as the PCM and air as the HTF to assess the thermal and flow characteristics during the charging process of the latent heat storage.
3. Demonstrate the utilization of a GCNN to predict the melt time and pressure drop in the flow through the macro-porous unit-cells, with the predictions improved over a simpler ANN using fields from the volume domain and the PCM-HTF interface fields.

## 2. Method

### 2.1. Macro-porous Unit-cells Generation

The procedure of generating computational fluid dynamics (CFD) meshes for macro-porous unit-cells with random and ordered sub-structures from a 3D stack of artificial tomography data are detailed in Fig. 1. For the random sub-structures, a stack of random pixels images  $150 \times 150 \times 400$  pixels<sup>3</sup>, shown in Fig. 1a, was generated by randomly assigning binary values (0 or 1) at each voxel. The size of the stack is large enough to represent a periodic cell of the macro-porous structure with a wide range of porous sub-structure length scales while being limited by the memory for further conversion into meshes. This stack was passed through a 3D Gaussian filter with different kernel sizes (between 5 and 30 pixels) depending on the length scale of the porous sub-structures required and normalized. A final porosity filter acts as a threshold to generate a 3D image stack of the structures with the required porosity. This process of generating random sub-structures was automatized to generate 1163 3D meshes with varying sub-structure length scales and porosity as detailed in the Section 3.1, as the accuracy of GCNNs has been observed to plateau only with sample numbers larger than 1000 [58]. For the ordered sub-structures, points were positioned in a cubic arrangement separated by a constant distance and connected by straight lines to obtain a skeletal structure. This cubic arrangement was converted into a stack of images  $150 \times 150 \times 400$  pixels<sup>3</sup> by adding pixelated spheres of required strut diameters along each connecting line in the cubic arrangement to create 3D image stacks shown in Fig. 1b. 68 such ordered sub-structures were constructed with different cubic based arrangements (2x2x2 to 4x4x4), range of strut diameters (5 to 15 pixels), and cross-linkages within the structure. To simulate a unit-cell of the latent heat storage, a fully connected 3D percolating monolithic PCM is required to be physically reproducible, for example by 3D printing. Using the open source 3D image processing package Fiji [59], STL

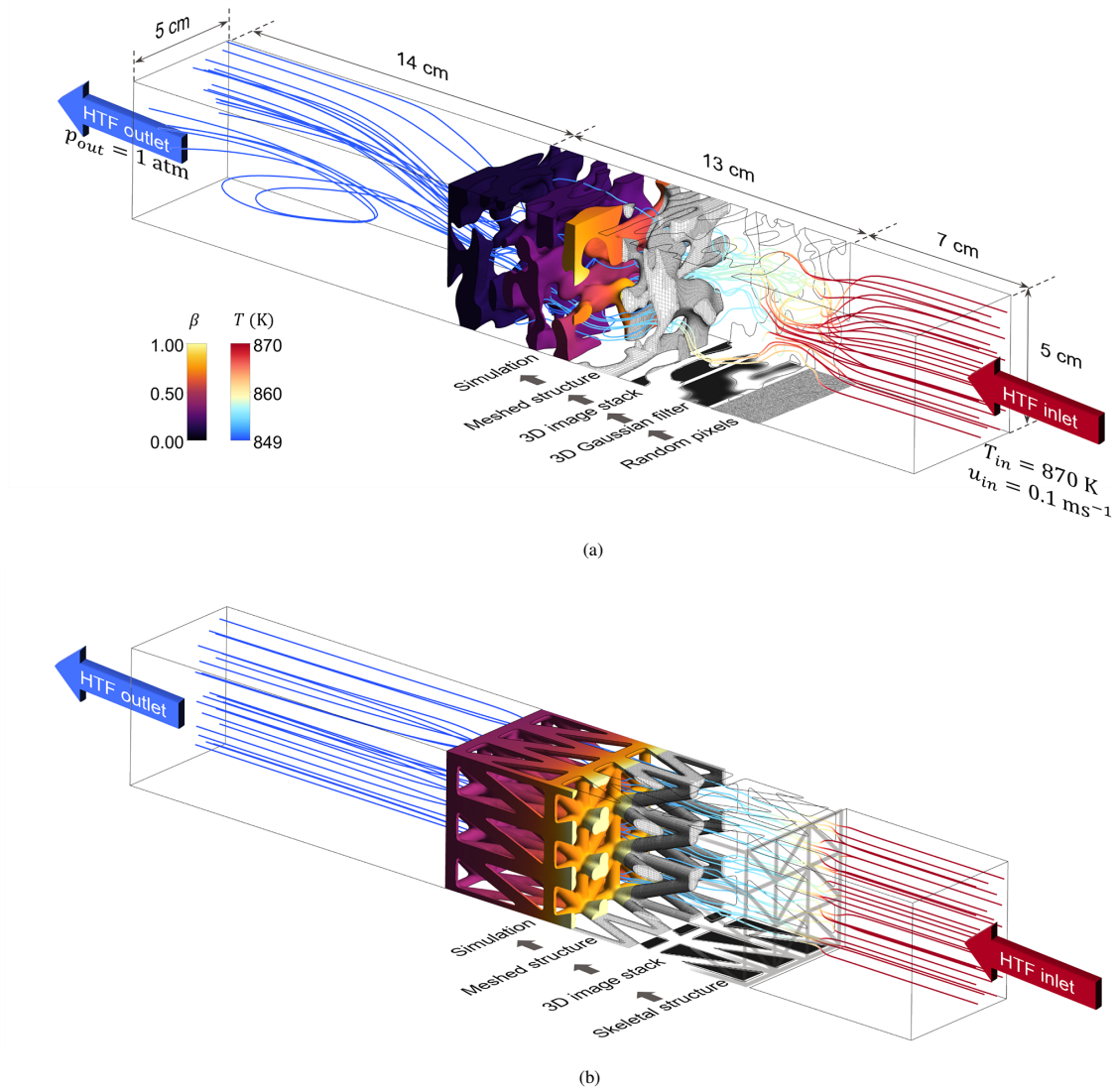


Figure 1: Unit-cells of 3D monolithic macro-porous structures showing the dimensions, flow direction for the HTF, and the steps for generating the unit-cells with (a) random and (b) ordered sub-structures. The simulation results on the CFD mesh generated using the structures are shown as velocity streamlines colored by temperature,  $T$ , and melt fraction,  $\beta$ , of the PCM.

meshes were obtained from the image stacks and processed using the 3D software Blender [60] to remove the physically disconnected regions and obtain a monolithic surface mesh STL file. This actually reduced 4000 initially created structures to the 1'163 structures usable for the analysis. Finally, the open source meshing code *snappyHexMesh* in OpenFOAM [61] was used to generate hexahedral meshes from the STL files with multi-layer refinements close to the interfaces as shown in Fig. 1. Details of the generation procedure are provided in supplementary section. The hexahedral meshes were scaled to the dimensions  $5 \times 5 \times 13 \text{ cm}^3$  to depict realistic dimensions usable in the LHTES setup [5], with the unit-cells generated representing a periodically replicated unit-cell of a larger latent heat storage structure.

## 2.2. Numerical Model

A 3D coupled CFD-heat transfer model developed in ANSYS Fluent was used to perform the phase change simulations

on the percolating macro-porous unit-cells during charging. A similar heat transfer and phase change behavior is expected during the discharging process. The aluminum alloy  $\text{Al}_{87.4}\text{Si}_{12.6}$  (wt%) [4] was used as the PCM, with air, behaving as an ideal gas, as the HTF. We assumed:

1. The thin encapsulation layer over the structures was neglected for the simulation as it does not significantly contribute to the phase change evolution. Sensible heat stored within the simulation temperature bounds with a 1 mm thick encapsulation accounts for 4.4% of the total energy stored in the structure for the largest surface area cases. The contribution of the thin layer of encapsulation to the thermal resistance is dependent on the encapsulation material and is not considered.
2. The PCM is homogeneous and isotropic. Temperature and phase dependent specific heat capacity and thermal conductivity for  $\text{Al}_{87.4}\text{Si}_{12.6}$  during phase change (as listed in



Tab. 1) are simulated using point-wise linear interpolation.

3. The effect of buoyant convection inside the PCM is neglected, according to results of high conductivity PCMs [62, 4] at low Stefan numbers. Thus no explicit tracking of the melt interface within the PCM was required. The molten PCM is modeled as a solid.
4. Radiative heat transfer within the porous structure and thermal expansion of the PCM was neglected as the initialization temperature of the simulation domain is close to the inlet temperature of the HTF (to skip the slow sensible heating of the structure) resulting in small temperature differences between the macro-porous unit-cell and the HTF.

The momentum conservation equation solved in the computational domain of the HTF is:

$$\frac{\partial}{\partial t}(\rho_{\text{air}}\mathbf{u}) + \nabla \cdot (\rho_{\text{air}}\mathbf{u}\mathbf{u}) = -\nabla P + \nabla \cdot \boldsymbol{\tau} + \rho_{\text{air}}\mathbf{g} + \mathbf{F} \quad (1)$$

where  $\rho_{\text{air}} = p/R_{\text{air}}T$  for the ideal gas,  $\boldsymbol{\tau}$  is the shear stress tensor, and  $\mathbf{F}$  is the external body force from interaction with the solid PCM domain. The energy equation in the HTF domain is:

$$\frac{\partial}{\partial t}(\rho_{\text{air}}h_{\text{air}}) + \nabla \cdot (\mathbf{u}(\rho_{\text{air}}h_{\text{air}} + P)) = \nabla \cdot (k_{\text{air}}\nabla T) + \dot{q} \quad (2)$$

where  $h_{\text{air}} = c_{p,\text{air}}\Delta T$  is the enthalpy of the ideal gas, and  $\dot{q}$  is the convective heat transfer interaction with the PCM. The energy equation in the solid PCM domain is:

$$\frac{\partial}{\partial t}(\rho_{\text{pcm}}h_{\text{pcm}}) = \nabla \cdot (k_{\text{pcm}}\nabla T) - \dot{q} \quad (3)$$

where enthalpy  $h_{\text{pcm}} = \int c_{p,\text{pcm}} dT$ . The phase change inside the PCM is modeled using the effective heat capacity method which uses an increased specific heat capacity [63] of the PCM within the phase change temperature range to account for the latent heat. The latent heat is assumed to be added to the specific heat linearly with temperature during phase change:

$$c_p = \begin{cases} c_{p,s} & T < T_s \\ c_{p,s} + \beta(c_{p,l} - c_{p,s}) + \frac{L}{T_l - T_s} & T_s \leq T \leq T_l \\ c_{p,l} & T > T_l \end{cases}$$

The macro-porous unit-cells were simulated for charging using a constant velocity  $u_{\text{in}} = 0.1 \text{ ms}^{-1}$  laminar influx (Reynolds number of 250 based on the channel size of 5 cm) of the HTF maintained at a constant inlet temperature of  $T_{\text{in}} = 870 \text{ K}$  with the exit maintained at a constant pressure of  $p_{\text{out}} = 1 \text{ atm}$ . The remaining four boundaries were set as symmetry boundary condition so that the structure represents a unit periodic cell of a larger heat storage. The simulation was initialized at 845 K to skip most of the the sensible heating part of the simulation and thus reduce computational time. Nevertheless if the sensible simulation was performed, the combination of a latent heat storage (200x) compared to the sensible heat storage and the limiting HTF-PCM convective heat transfer will result in a near-uniform temperature within the macro-porous structure.

The simulation setup was solved in ANSYS Fluent with settings detailed in the supplementary section. The simulation results at 10'000 s, when all structures were still in the process of phase change, were exported as temperature,  $T$ , pressure,  $P$ , and velocity,  $u$ , distributions on a volume mesh,  $X_{\text{vol}}$ , of size  $40 \times 40 \times 400$ , and heat flux,  $\dot{q}$ , and shear stress,  $\tau$ , field distributions on a surface mesh,  $X_{\text{surf}}$ .

The latent energy stored by the macro-porous unit-cell can be expressed as  $\rho_{\text{pcm}}LV_{\text{pcm}} = \rho_{\text{pcm}}LV_{\text{tot}}(1 - \phi)$ , where  $\phi$  is the porosity and  $V_{\text{tot}}$  represents the volume of the bounding box within which the various macro-porous unit-cells are created ( $5 \times 5 \times 13 \text{ cm}^3$  in Fig. 1). The mean heat transfer rate or power can be defined as:  $\rho_{\text{pcm}}LV_{\text{pcm}}/t_{\text{melt}} = \rho_{\text{pcm}}LV_{\text{tot}}(1 - \phi)/t_{\text{melt}}$ . The melt time  $t_{\text{melt}}$  obtained from the phase change simulations thus represents the ratio of energy to power rating of the macro-porous unit-cell. A normalized melt time,  $t_{\text{norm}}$ , was used to compare the melting time for each unit-cell for the same input flow enthalpy of HTF:

$$t_{\text{norm}} = \frac{t_{\text{melt}}}{(1 - \phi)} \cdot \frac{\dot{m} c_{p,\text{air}} (T_{\text{in}} - T_{\text{m}})}{\rho_{\text{pcm}} L V_{\text{tot}}} \quad (4)$$

A smaller  $t_{\text{norm}}$  is thus an indication of a higher relative power density of the macro-porous unit-cell.

The specific heat capacity model has been validated experimentally in a previous work [5] with a test-bed for high-temperature latent heat storage using cylindrical encapsulated aluminium alloy surrounded by ceramic porous media. The pressure drops calculated by the simulations have been verified to have the same order of magnitude as pressure drops obtained using correlations for ceramic and metal sponges [65, 6], cylindrical arrays [66], fibrous beds [67], and packed beds of spherical particles [68, 69].

### 2.3. Deep Learning Based Physics Emulators

#### 2.3.1. Naive Network - ANN

A fully connected artificial neural network (ANN) was created to use as a standard regressor, with only the macroscopic properties as input and the scalars  $t_{\text{melt}}$ ,  $t_{\text{norm}}$  and  $\Delta P$  as outputs. The ANN was compared with the performance of the GCNN. The ANN shown in Fig. 2 is comprised of 8 layers with 20 neurons in each layer with ReLU (Rectified Linear Units) activation at each neuron to limit the output values of each neuron between 0 and 1. The particular selection of layers and number of neurons was chosen by trial-and-error to obtain the best results without overfitting (divergence of test set  $r^2$  values). Normalization and scaling to unit variance was performed on the inputs and outputs for better convergence, and Gaussian noise was added to the inputs for regularization before training. A least square error regularization is also performed at each neuron to prevent overfitting. L2 (least square error) loss was used for the scalars predictions. The inputs to the ANN consisted of the macro-porous unit-cell properties, namely  $\phi$ ,  $A$ , and a two-point surface-void correlation functions,  $F_{sv}$  detailed in the supplementary section.

$\text{Al}_{87.4}\text{Si}_{12.6}$				
Temperature $T$ (K)	Density $\rho$ ( $\text{kg m}^{-3}$ )	Thermal Conductivity $k$ ( $\text{W m}^{-1} \text{K}^{-1}$ )	Specific Heat Capacity, $c_p$ ( $\text{J kg}^{-1} \text{K}^{-1}$ )	Viscosity $\mu$ (Pa s)
273	2700.0	160	1070	-
849 ( $T_s$ )	2587.5	160	1070	-
851 ( $T_l$ )	2460	70	1170	$1.30 \times 10^{-3}$
950	2428.1	70	1170	$1.30 \times 10^{-3}$

Table 1: Temperature and phase-dependent properties of  $\text{Al}_{87.4}\text{Si}_{12.6}$  [2, 64] with latent heat of melting  $L = 470 \text{ kJ kg}^{-1}$ .

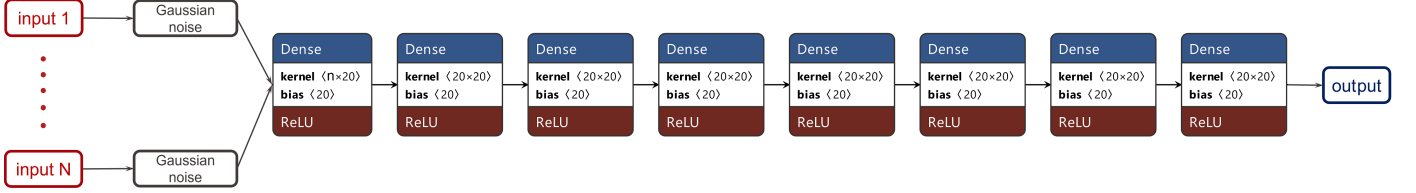


Figure 2: ANN architecture showing four layers of the dense (fully connected) network with ReLU activation at each neuron.

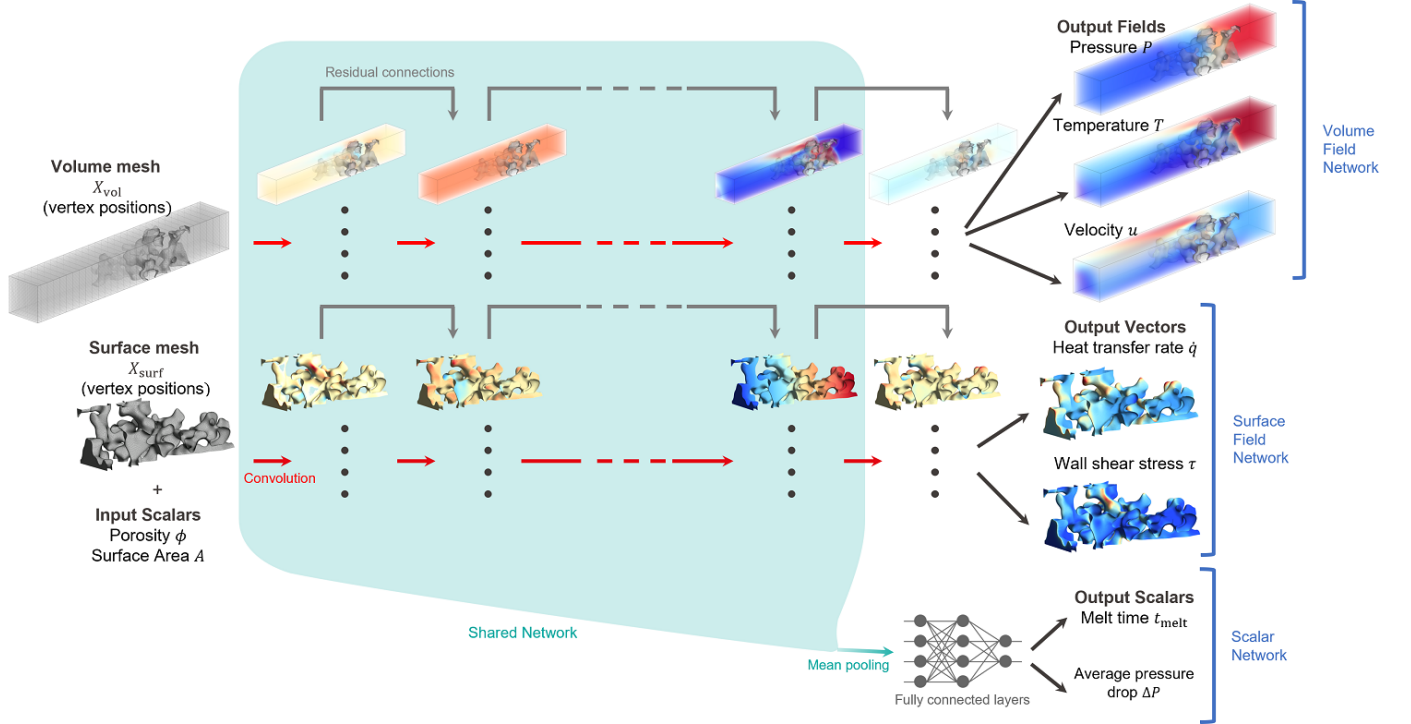


Figure 3: GCNN architecture showing the convolutional volume and surface field networks, and the fully connected scalar network, with input/output mesh, output fields and scalars.

### 2.3.2. Geodesic Convolutional Neural Network (GCNN)

A GCNN was designed to predict the output scalar values of  $t_{\text{melt}}$ ,  $t_{\text{norm}}$ , and  $\Delta P$ , obtained from the simulations. Macroscopic properties porosity,  $\phi$ , and surface area,  $A$ , calculated from the macro-porous unit-cells are provided as scalar inputs along with the meshes  $X_{\text{vol}}$  and  $X_{\text{surf}}$ . The GCNN network architecture has separate volume and surface field network, and scalar network to predict the volume field outputs  $T$ ,  $P$ , and  $u$ , surface field outputs  $\dot{q}$  and  $\tau$ , and scalar outputs  $t_{\text{norm}}$  and  $\Delta P$ ,

with a few initial layers shared by the field and scalar networks connected via a mean pooling operation. The  $t_{\text{melt}}$  was calculated from  $t_{\text{norm}}$  using eqn. 4. Fig. 3 details the GCNN architecture used with intermediate level features also shown. The volume and surface field networks constitute mesh convolution operations at each layer, whereas the network to predict scalar outputs is based on fully connected network layers. The data at both, input and output, are either z-score or log normalized, depending on their distribution and scaled to unit variance before

being used in the GCNN to speed up the convergence. L1 (least absolute error) losses were used for the scalars and L2 (least square error) losses were used for the fields, due to outliers being present in  $\Delta P$ . The losses for the fields were weighted 5 times larger than the scalars for the combined loss to prevent overfitting of the scalars. A larger value of the weights would result in a delayed convergence of the  $r^2$  value requiring more iterations for training.

### 3. Results

#### 3.1. Macro-porous Structure Characterization

Even though the macro-porous unit-cells cannot be explicitly described by a few parameters only, macroscopic properties of the structures - like  $\phi$  and  $A$  - can be obtained. Fig. 4 shows the distribution of these macroscopic properties as a function of  $t_{\text{melt}}$ ,  $\Delta P$ ,  $\langle \dot{q} \rangle$  and  $\langle \tau \rangle$  for each structure obtained from the simulations. The figure also displays the topology of a few, select unit-cells with random and ordered sub-structures. Fig. 5 shows their distribution compared to the mean of the volume fields  $\langle T \rangle$ ,  $\langle P \rangle$ , and  $\langle u \rangle$ . Figs. 4 and 5, while displaying the range of macro-porous structures generated using the porous media generation technique detailed in this paper, also depict the applicability range of the trained deep learning models used in this paper. A z-score normalization is performed on all the variables before being input into the ANN and GCNN networks, except for  $\Delta P$  and  $P$  which are log normalized as their values are spread over a large range of orders of magnitudes, shown by their distribution plots in Fig. 4 and Fig. 5. Note that only a few random sub-structured unit-cells are present in the data set at large  $\phi$  because of the random structure generation process where several disconnected regions or air pockets are often formed at high porosities which end up being removed, thus generally resulting in a dataset with lower  $\phi$  structures. Fig. 6 shows a plot of the opposing scalar outputs  $t_{\text{norm}}$  vs  $\Delta P$  for the random and ordered structures. The Pareto fronts shown in Fig. 6 indicate that ordered structures outperform the random structures. It is seen from the distribution plots of  $A$  and  $\phi$  in Fig. 4 that there is a lack of random structures with large  $A$  at high  $\phi$  which could explain some of the under-performance compared to the ordered structures. However, the higher thermal-fluid performance of the ordered structure is due to better heat transfer fluid flow management preventing clogged flow sections often seen in random structures. This shows that the overall transport properties of the macro-porous structures are not only a function of the macro-porous properties like surface area, porosity, and cell size but also dependent on the geometrical anomalies which can deviate the flow path. The set of structures generated have a range of macroscopic properties  $\phi = 0.23 - 0.95$  and  $\phi = 0.41 - 0.96$ ,  $A = 0.005 - 0.064 \text{ m}^2$  and  $A = 0.013 - 0.076 \text{ m}^2$  for random and ordered structures respectively. The output scalars are in the range  $t_{\text{melt}} = 13'400 - 125'100 \text{ s}$  and  $t_{\text{melt}} = 6'680 - 92'830 \text{ s}$ ,  $\Delta P = 0.0078 - 169 \text{ Pa}$  and  $\Delta P = 0.020 - 3.149 \text{ Pa}$  for random and ordered structures respectively. The data set of random and ordered sub-structures are not exhaustive but represent a large range of the domain of possible unit-cell structures.

The predictions by simple linear and exponential fitting for  $t_{\text{melt}}$  and  $\Delta P$  are shown as red lines with  $r^2$  values in the corresponding plots.  $t_{\text{melt}}$  is predicted with  $r^2 = 0.968$  using a linear fit with  $\phi$  ( $t_{\text{melt}} = 153'431.62 - 145'224.92 \cdot \phi$ ) and  $t_{\text{norm}}$  is predicted with  $r^2 = 0.708$  using an exponential fit with  $A$  ( $t_{\text{norm}} = 1.0152 + 1.5310 \cdot e^{-161.803 \cdot \phi + 1.1117}$ ). An exponential fitting against  $\phi$  for  $\Delta P$  results in  $r^2 = 0.200$  as shown in Fig. 4 ( $\Delta P = 0.1293 + 1.9588 \cdot e^{-11.4197 \cdot \phi + 5.2836}$ ). The exponential fit is much better ( $r^2 = 0.644$  using  $\Delta P = -6.6097 + 1.0704 \cdot e^{36.9922 \cdot \langle \tau \rangle + 1.6605}$ ) with  $\langle \tau \rangle$  for  $\Delta P$ . The mean fields  $\langle P \rangle$  and  $\langle u \rangle$  also correlate with  $\Delta P$  linearly  $r^2 = 0.856$  ( $\Delta P = 0.1284 + 3.7635 \cdot \langle P \rangle$ ) and exponentially  $r^2 = 0.784$  ( $\Delta P = -2.9133 + 0.6321 \cdot e^{18.7763 \cdot \langle u \rangle + 0.7963}$ ) respectively.  $A$  correlates exponentially with  $\langle \dot{q} \rangle$  ( $r^2 = 0.783$  using  $\langle \dot{q} \rangle = 15.8302 + 6.9111 \cdot e^{-31.7358 \cdot A + 3.1070}$  in Fig. 4) and  $\langle T \rangle$  ( $r^2 = 0.281$  using  $\langle T \rangle = 849.6496 + 1.8469 \times 10^{-2} \cdot e^{-84.9948 \cdot A + 6.5658}$  in Fig. 5) which would aid the GCNN in predicting both,  $t_{\text{melt}}$  and  $\Delta P$ . These correlations justify the usage of the volume and surface fields in the GCNN to better predict the output scalars  $t_{\text{melt}}$  and  $\Delta P$ .

#### 3.2. Training: ANN

The ANN was trained on a randomly chosen test set consisting of 90% of the macro-porous unit-cells and the remaining 10% of the unit-cells constituted the test set for validation and overfitting check of the model. The scalars  $t_{\text{melt}}$ ,  $t_{\text{norm}}$  and  $\Delta P$  were predicted individually using separate ANNs. Training was performed with different inputs: with only  $\phi$  and  $A$  as inputs named as ANN-scal, and with  $F_{sv}$  correlation function additionally as input named as ANN-corr. Training was performed for 2000 iterations (around 4 to 5 minutes on a single NVIDIA GeForce GTX 750 Ti GPU) with batch sizes of 30 for both the models, with ANN-scal and ANN-corr, consisting of around 3000 to 4500 parameters to fit during training.

The results of the trained ANN-scal and ANN-corr are shown in the ground truth vs prediction plots of Fig. 7, where perfect predictions with  $r^2 = 1$  results in all the points coinciding with the dashed diagonal line.  $t_{\text{melt}}$ ,  $t_{\text{norm}}$ , and  $\Delta P$  are better predicted (with an increase in accuracy of 1.76%, 14.3% and 125.5%) using the ANN-corr compared to the linear/exponential fitting with the input scalars. The predictions of  $t_{\text{norm}}$  and  $\Delta P$  were improved by using  $F_{sv}$  correlation values in addition to  $\phi$  and  $A$  as observed when comparing Fig. 7c and Fig. 7f. The set of 75  $F_{sv}$  correlation values provided a succinct numerical representation of the macro-porous unit-cell to the ANN in addition to the  $\phi$  and  $A$  values, which improve the predictions of the output scalars  $t_{\text{melt}}$ ,  $t_{\text{norm}}$ , and  $\Delta P$  (by 0.1%, 5.20%, and 173% compared to the ANN-scal, respectively). Attempts of using other macroscopic properties like tortuosity, mean pore diameter, chord lengths, etc., or two-point functions such as void-void, and surface-surface correlations [70] did not further improve the training results. This was in contrast to a study using ANNs to predict oxygen generation in a solar-driven porous thermochemical reactors using macroscopic properties of the porous media observed where significant improvement in predictions were observed using the inputs tortuosity, surface-void, void-void, and surface-surface correlations [54].

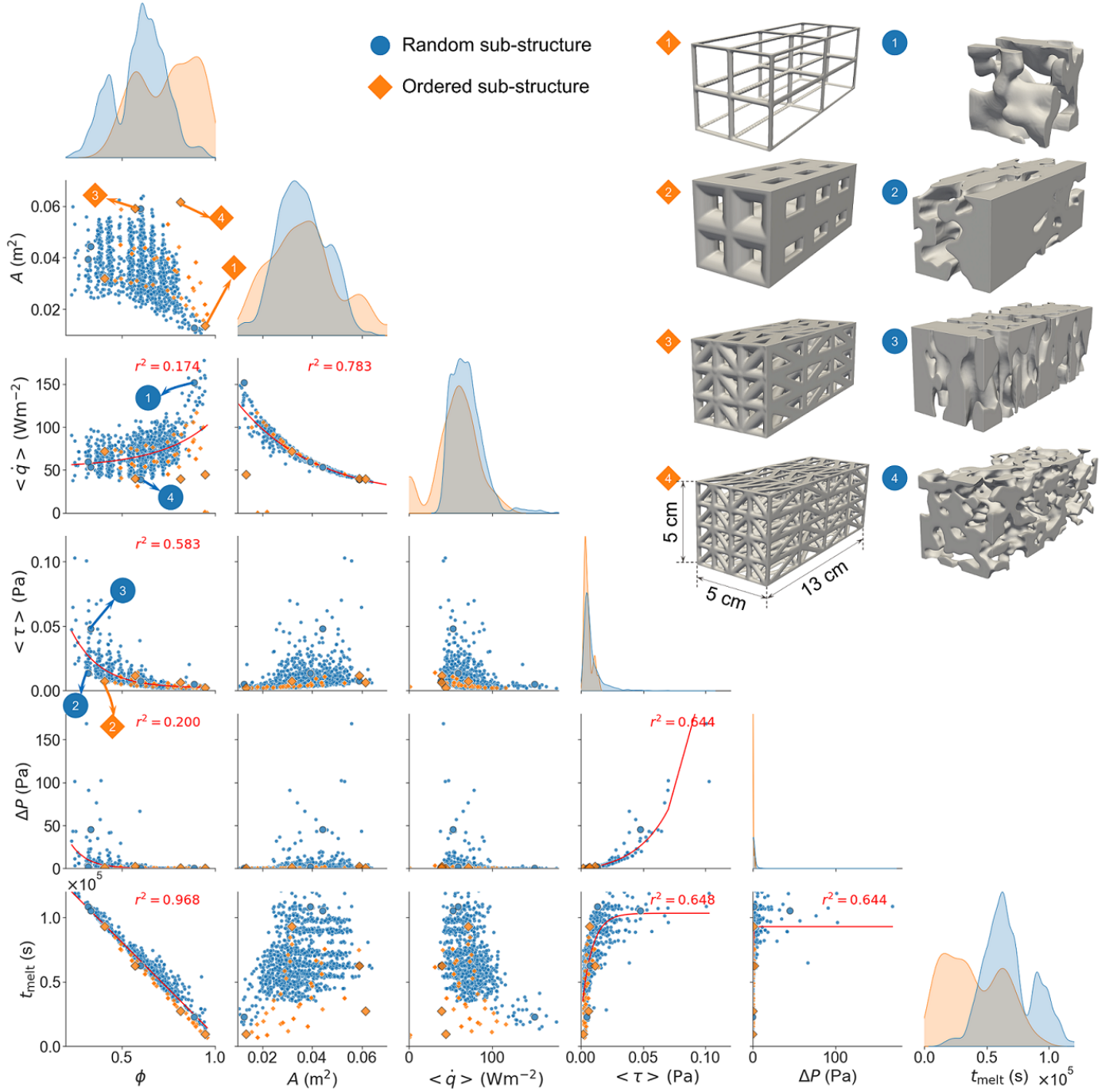


Figure 4: Distribution and relative variation of macroscopic properties -  $\phi$  and  $A$  - from the characterization and results from the simulations -  $t_{\text{melt}}$ ,  $\Delta P$ , mean values of the heat flux,  $\langle \dot{q} \rangle$ , and shear stress,  $\langle \tau \rangle$ , fields on the interface surface mesh of the macro-porous unit-cells - for random (blue) and ordered (orange) sub-structures. The red lines are linear and exponential fits with the corresponding  $r^2$  value mentioned in the plots. A few example random and ordered sub-structure unit-cells are displayed and marked in each plot.

### 3.3. Training: GCNN

The GCNN training was performed with a batch size of 1 (due to the limited GPU memory and large sizes of the surface and volume meshes) for 500'000 iterations (after which the  $r^2$  values converged) with 90% of the structures used for training set with the remaining structures used for the test set. The learning rate of 0.001 which exponentially decays to 0.9x its value every 10'000 steps was chosen such that the parameters of the

network are explored in a large enough domain while maintaining stable convergence of the training accuracy. The training required around 300hrs of computation on a Tesla-K80 GPU by NVIDIA. Fig. 8 shows the ground truth vs prediction plots for the output scalars using the GCNN. The comparison of test set prediction accuracy from the different methods - simple linear/exponential fitting, ANN-scal, ANN-corr, and GCNN are summarized in the Table 2.



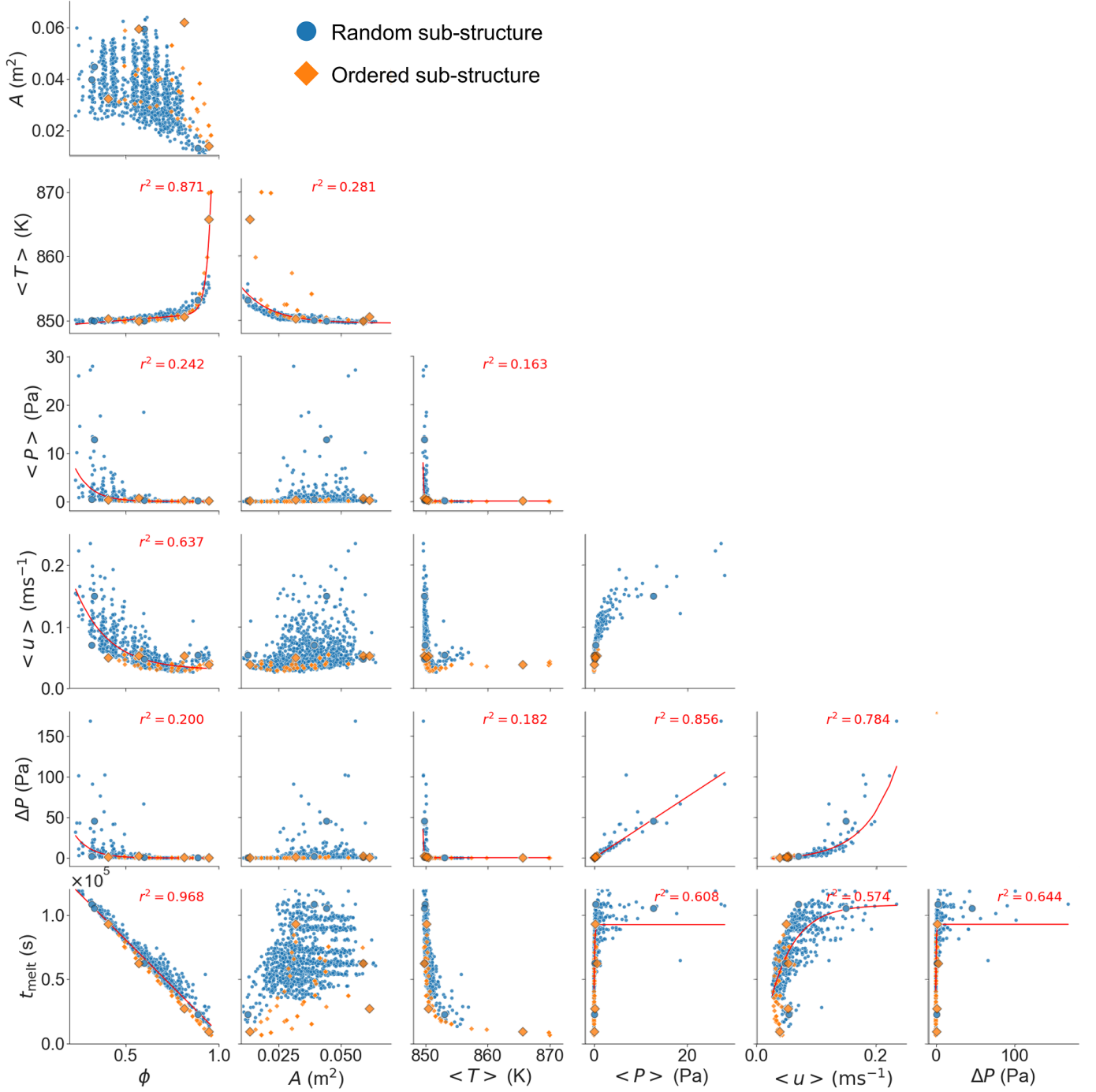


Figure 5: Distribution and relative variation of macroscopic properties -  $\phi$  and  $A$  - from the characterization and results from the simulations -  $t_{\text{melt}}$ ,  $\Delta P$ , mean values of temperature  $\langle T \rangle$ , pressure  $\langle P \rangle$  and velocity  $\langle u \rangle$  fields in the volume mesh of the macro-porous unit-cells - with random (blue) and ordered (orange) sub-structures. The red lines are the linear and exponential fits with the corresponding  $r^2$  value mentioned in the plots.

The output scalars  $t_{\text{melt}}$ ,  $t_{\text{norm}}$ , and  $\Delta P$  are all better predicted (with increase in accuracy of 2.38%, 6.78%, and 352%) using the GCNN compared to the linear/exponential fitting. The prediction of  $\Delta P$  outperforms the ANN-corr by a large margin, due to the presence of the volume and surface field networks which act as regularizers for the fully connected scalar networks and also prevent overfitting by adding correlated information to train an ill-posed problem. Note that the training

sets in GCNN (Fig. 8) for both the output scalars are better predicted than the training sets in ANN (Fig. 7), which emphasizes the importance of fields being trained alongside the scalars. Using fields as regularizers and forcing the network to learn data consistent and relevant to the predictions has thus been found to be helpful to better train the network while preventing uncontrolled extrapolation of the output scalars. This technique of improving learning by predicting additional relevant quantities

Model	$r_{t_{\text{melt}}}^2$	$r_{t_{\text{norm}}}^2$	$r_{\Delta P}^2$	$r_T^2$	$r_P^2$	$r_u^2$	$r_{\dot{q}}^2$	$r_{\tau}^2$
Linear/Exponential Fit	0.968	0.708	0.200					
ANN-scal	0.984	0.769	0.165					
	(1.65%)	(8.62%)	(-17.5%)					
ANN-corr	0.985	0.809	0.451					
	(1.76%)	(14.3%)	(125.5%)					
GCNN	0.991	0.756	0.904	0.930	0.605	0.142	0.695	0.210
	(2.38%)	(6.78%)	(352.0%)					

Table 2: Comparison of test-set prediction accuracy of the different scalars, volume and surface fields using simple fitting, ANN and GCNN. The increase or decrease in accuracy over the linear/exponential fitting is shown in percentage below the  $r^2$  values.)

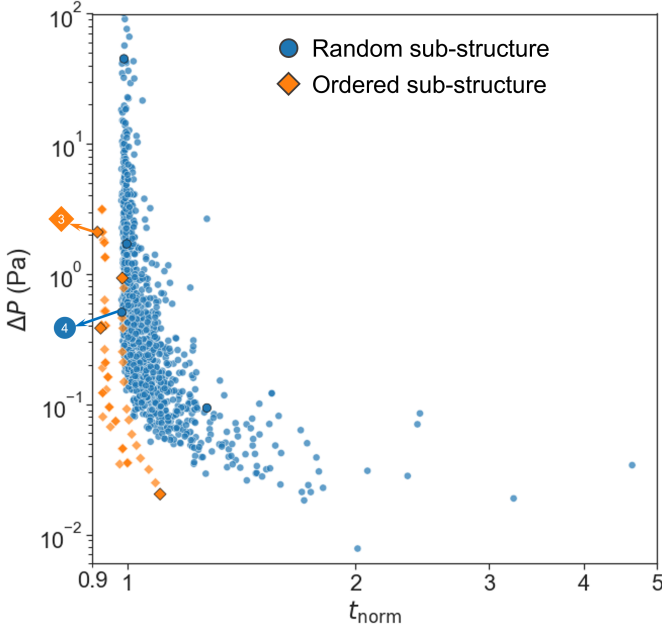


Figure 6:  $t_{\text{melt}}$  and  $\Delta P$  values from the simulations for the different macro-porous unit-cells with random (circles) and ordered (diamonds) sub-structures.

through connected training branches, called disentangling [71], has been studied for deep learning applications such as facial recognition [72] and drug-discovery [73]. Disentangling also results in intermediate level features (as shown in Fig. 3) is less prone to overfitting.

In addition to predicting the required scalars, Figs. 9 and 10 demonstrate the usage of the GCNN as a coupled CFD-heat transfer emulator comparing the ground truth, prediction and the relative difference percentage error (at each node in the mesh) for volume and surface fields in two macro-porous unit-cells, a random and an ordered sub-structure both located on the Pareto front of Fig. 6. The prediction accuracy are listed for each figure and averaged for all samples in the Table 2. On average, the  $T$  fields are predicted with high accuracy of 93% followed by  $\dot{q}$  at 69.5% and  $P$  at 60.5%. Large prediction errors up to 57% in  $P$  field predictions are observed at the domain inlet as shown in Figs. 9b and 10b, where higher  $P$  values are present in the domain. The average prediction accuracy is lower (14.2%) for  $u$  fields with errors observed after the macro-porous structure due to formation of vortices and back-

flows from the exit. Larger errors for  $u$  fields are observed for the ordered structure (for example in Fig. 10c) due to higher velocity values observed in the ordered structures with high  $\phi$ . Prediction accuracy of  $\tau$  correlated with the  $u$  fields and were also low, averaging at 21.0%. The predictions for  $P$ ,  $u$  and  $\tau$  can be improved either by using additional volume field scalar inputs like time of flight [57], adding data about the shortest distance of points in the domain from the inlet [74], or by using physics based GCNNs - for example, by adding loss functions based on correlations between the  $u$ ,  $\tau$  and  $P$  fields. Nevertheless, these results obtained from the test sets confirm that the GCNN architecture is learning physical phenomena as a coupled CFD-heat transfer emulator and not just interpolating the volume and surface fields.

The trained GCNN can thus be used as a surrogate model or proxy for the 3D CFD simulator to evaluate the outputs, i.e.,  $T$ ,  $P$ ,  $u$ ,  $\dot{q}$ ,  $\tau$ ,  $t_{\text{melt}}$ ,  $t_{\text{norm}}$ , and  $\Delta P$ . Although the intermediate level features of the GCNN predict volume and surface distributions, they are training dependent and do not represent any meaningful physical quantity of the modelled system. Meaningful physical intermediate features could be created in physics based GCNN models where Navier-Stokes based loss functions are used [42]. The GCNN network, being a combination of linear regressors, is differentiable with respect to coordinates of the vertices in the  $X_{\text{surf}}$ , and  $X_{\text{vol}}$ , meshes. A gradient-based technique can further be used to minimize both the pressure drop and normalized melting time by moving the mesh vertices in contrast to the ANNs which do not consider explicit geometric information of the structures. Ordered and random structures on the Pareto front of Fig. 6 could be modified using 3D Gaussian kernel based movements added on randomly chosen vertices of the structures. Heuristic optimization methods can be used to choose the structures based on the optimization fitness criteria and modify them further. The optimization process can also incorporate design constraints such as limiting the  $\phi$  to a given range, the presence of contacts on all four walls of the unit-cell, sustaining a minimum distance between the monolithic mesh vertices to maintain minimum thickness of the percolating macro-porous unit-cells, space allowance for addition of encapsulation, and prevent obstruction to the HTF flow. The trained GCNN network predicts the specific scalars and fields at a particular time step with specific boundary conditions. The GCNN could be generalized to further include boundary conditions and thermal properties of the PCM and HTF as inputs

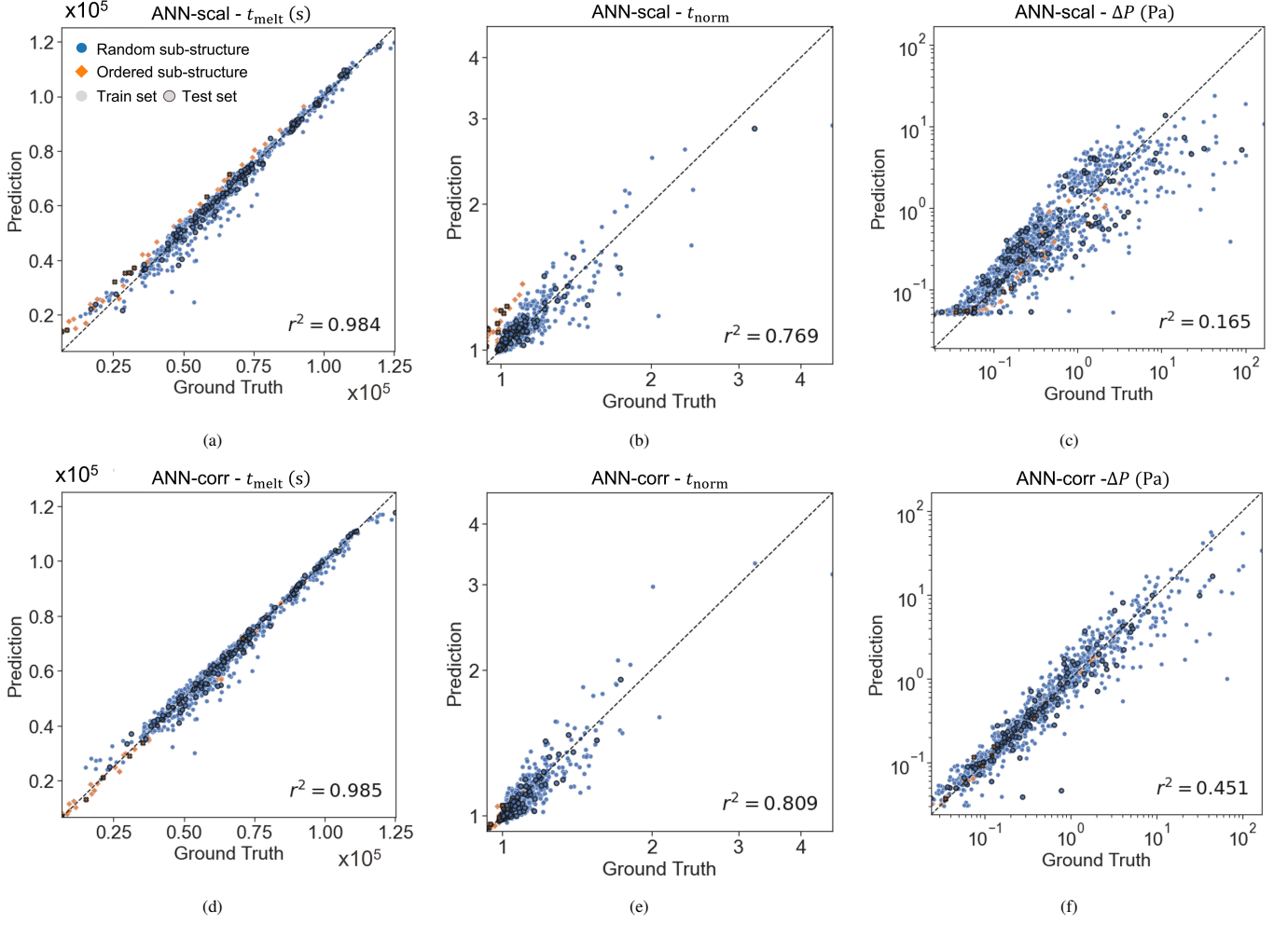


Figure 7: Ground truth vs prediction plots for  $t_{\text{norm}}$  (a and d),  $t_{\text{melt}}$  (b and e) and  $\Delta P$  (c and f) using the ANN-scal (a - c) and ANN-corr (d - f) with random (blue) and ordered (orange) sub-structures.

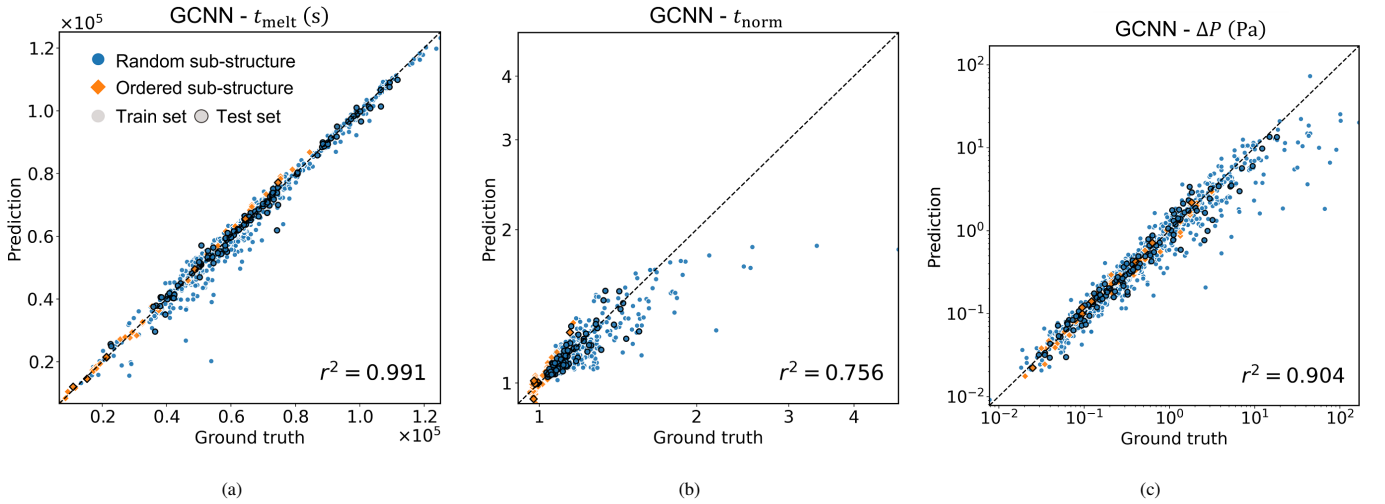


Figure 8: Ground truth vs prediction plots using the GCNN for (a)  $t_{\text{norm}}$ , (b)  $t_{\text{melt}}$  and (c)  $\Delta P$  for the macro-porous unit-cells with random (blue) and ordered (orange) sub-structures.

to the network. A combination of the GCNN and the time-series predicting Recurrent Neural Networks [75] can be used

to also extend the GCNN application as a surrogate transient CFD simulator which will also lead to better prediction of the

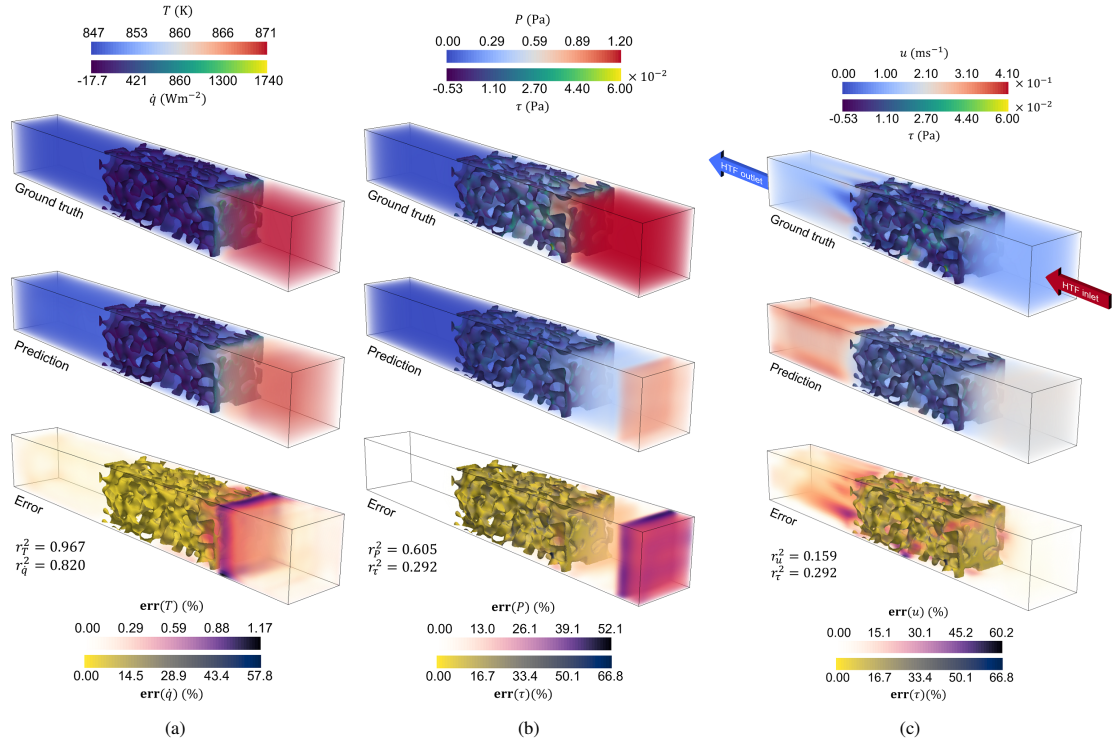


Figure 9: Ground truth, prediction, and relative difference error in % for (a)  $T$  and  $\dot{q}$ , (b)  $P$  and  $\tau$ , and (c)  $u$  and  $\tau$  fields and their corresponding  $r^2$  values for a random macro-porous unit-cell (random sub-structure listed as 4 in Fig. 4) using the GCNN.

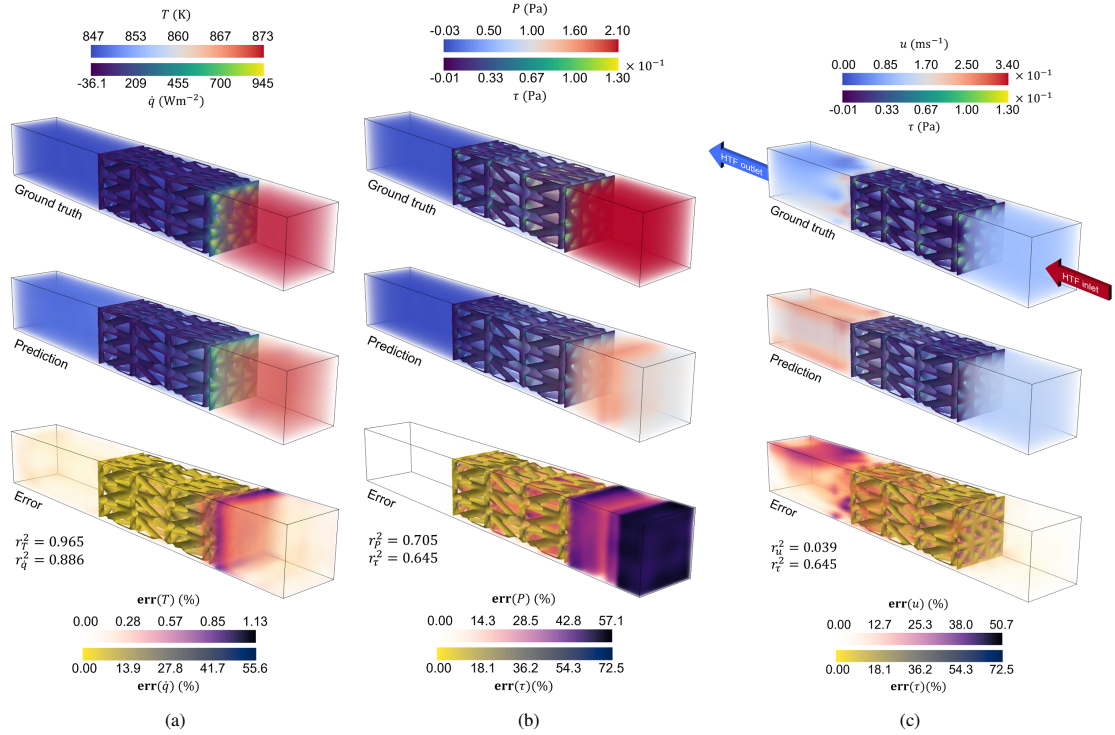


Figure 10: Ground truth, prediction, and relative difference error in % for (a)  $T$  and  $\dot{q}$ , (b)  $P$  and  $\tau$ , and (c)  $u$  and  $\tau$  fields and their corresponding  $r^2$  values for the ordered macro-porous unit-cell (ordered sub-structure listed as 3 in Fig. 4) using the GCNN.



scalars. The L1 and L2 losses used in the current GCNN can be replaced by physics based losses to substantially improve predictions of the fields and thus the scalars.

#### 4. Conclusions

We created novel artificially generated percolating macro-porous periodically replicating unit-cells of latent heat storage systems with random and ordered sub-structures. 3D image stacks of artificial macro-porous structures were produced using combination of random 3D Gaussian filters and ordered cubic point and cross-linkage arrangements to obtain 1163 random and 68 ordered unit-cells with a wide range of macroscopic properties ( $\phi = 0.23 - 0.96$ ,  $A = 0.005 - 0.076 \text{ m}^2$ ) and sub-structure length scales.

As the macro-porous unit cells cannot be explicitly parametrized, the unit-cells were characterized with respect to their macroscopic properties: porosity  $\phi$ , surface area  $A$ , and two-point surface-void correlation functions  $F_{sv}$ . The image stacks were used to obtain 3D CFD hexahedral meshes and used to simulate a transient charging process with  $\text{Al}_{87.4}\text{Si}_{12.6}$  as the PCM and air as the HTF using effective heat capacity method. The simulations output scalar values were: melt time  $t_{\text{melt}}$ , normalized melt time  $t_{\text{norm}}$  and pressure drop  $\Delta P$  which are the principal design characteristics for a latent heat storage. The simulation fields output on the PCM-HTF interface surface were: shear stress  $\tau$ , heat transfer rate  $\dot{q}$ . The volume fields output in the entire simulation domain were: temperature  $T$ , pressure  $P$ , and velocity  $u$ . Simple linear and exponential fits using  $\phi$  and  $A$  predicted the output scalars  $t_{\text{melt}}$ ,  $t_{\text{norm}}$ , and  $\Delta P$  of each macro-porous unit-cell with accuracy of  $r^2 = 0.968$ ,  $r^2 = 708$  and  $r^2 = 0.200$ , respectively. While the  $t_{\text{melt}}$  was predicted with 96.8% accuracy using the fits,  $t_{\text{norm}}$  (70.8%) and  $\Delta P$  (20%) predictions required improvements as they were not just dependent on the macroscopic properties but also on the topology of the structures. The unit-cell characterization using simulation results also established that the output scalars were correlated with the mean values of the volume and surface fields indicating their use for improved prediction capabilities.

Artificial neural networks were trained as standard regressors to improve the output scalar predictions, with  $\phi$  and  $A$  used as inputs in ANN-scal and  $F_{sv}$  additionally used as input for ANN-corr. While ANN-scal did not significantly change the prediction accuracy, ANN-corr increased the prediction accuracy for  $t_{\text{melt}}$  by 1.76%,  $t_{\text{norm}}$  by 14.3%, and  $\Delta P$  by 125.5%. The addition of the two-point surface-void correlation functions  $F_{sv}$  provides the network with data pertinent to the surface topology of the unit cells.

A geodesic convolutional neural network (GCNN) was built consisting of convolutional network branches for volume meshes and surface meshes, and fully connected network branches for prediction of the output scalars with the multiple branches connected via shared initial layers. The volume and surface mesh of the unit-cells are used as inputs along with  $\phi$  and  $A$  as input scalars. The network was trained to emulate a coupled CFD-heat transfer simulation by predicting the

volume and surface fields, along with the scalar outputs. Significant increase in prediction accuracy was demonstrated for  $t_{\text{melt}}$  (2.38%),  $t_{\text{norm}}$  (6.78%), and  $\Delta P$  (352.0%) compared to the simple fits, outperforming the artificial neural networks. The GCNN demonstrates the disentangling property of neural network where improvements in training and regularization of predictions were observed by forcing the network to learn additional data relevant to the output scalars.

The well trained GCNN model represents a lightweight version of simulation software with the advantage of predicting phase change behavior instantly for different geometries. The framework can be further extended to predict different boundary conditions by using them as inputs, while encountering physical phenomena such as turbulence at higher velocities. As the network represents a massive combination of linear regressors, work is ongoing that applies gradient-based techniques to optimize the structure of the surface mesh topology for optimized or required combinations of the output scalars.

#### 5. Acknowledgments

This material is based upon work performed in cooperation with CTI Swiss Competence Center for Energy Research (SC-CER Heat and Electricity Storage). Part of this work was performed with the financial support of the National Research Program ‘‘Energy Turnaround’’ (NRP 70) of the Swiss National Science Foundation (SNSF) under Grant #153780. Further information on the National Research Program is available at [www.nrp70.ch](http://www.nrp70.ch).

#### Nomenclature

##### Abbreviations

ANN	Artificial Neural Network
CFD	Computational Fluid Dynamics
GCNN	Geometric Convolutional Neural Network
HTF	Heat Transfer Fluid
LHTES	Latent Heat Thermal Energy Storage
PCM	Phase Change Material

##### English symbols

$\Delta P$	pressure drop	Pa
$\dot{m}$	mass flow rate	$\text{kg s}^{-1}$
$\dot{q}$	heat flux	$\text{W m}^{-2}$
<b>err</b>	Relative difference error	%
$A$	surface area	$\text{m}^2$
$c_p$	specific heat at constant pressure	$\text{J kg}^{-1} \text{K}^{-1}$

$F$	force	$\text{N m}^{-2}$
$F_{sv}$	two-point surface-void correlation	—
$g$	acceleration due to gravity	$\text{m s}^{-2}$
$h$	specific enthalpy	$\text{J kg}^{-1}$
$L$	latent heat of melting	$\text{J kg}^{-1}$
$P$	pressure	Pa
$r^2$	coefficient of determination	—
$T$	temperature	K
$t_{\text{melt}}$	melting time	s
$t_{\text{norm}}$	normalized melting time	—
$u$	velocity	$\text{m s}^{-1}$
$V$	volume	$\text{m}^3$
$k$	conductivity	$\text{W m}^{-1} \text{K}^{-1}$

### Mathematical Functions

$\nabla$	Gradient function
$\Delta$	Difference function
$\langle \rangle$	Mean value function

### Greek Symbols

$\beta$	PCM liquid/melt fraction $\left( \frac{T - T_s}{T_l - T_s} \right)$	—
$\Gamma(x)$	void indicator	—
$\phi$	porosity	—
$\Pi(x)$	surface indicator	—
$\rho$	density	$\text{kg m}^{-3}$
$\tau$	stress-strain tensor	$\text{N m}^{-2}$

### Subscripts

air	air / HTF
l	liquidus point PCM
pcm	PCM
s	solidus point PCM
tot	total

### References

- [1] International Renewable Energy Agency (IRENA), 2019, Renewables 2019 Tech. Rep. October 2019.
- [2] Kenisarin, M. M., 2010, "High-temperature phase change materials for thermal energy storage," *Renewable and Sustainable Energy Reviews*, **14**(3), 4, pp. 955–970.
- [3] Binder, S., and Haussener, S., 2020, "Design guidelines for Al-12%Si latent heat storage encapsulations to optimize performance and mitigate degradation," *Applied Surface Science*, **505**, 3, p. 143684.
- [4] Mallya, N., and Haussener, S., 2021, "Buoyancy-driven melting and solidification heat transfer analysis in encapsulated phase change materials," *International Journal of Heat and Mass Transfer*, **164**, 1, p. 120525.
- [5] Mallya, N., Suter, C., Binder, S., Barbato, M., Ortona, A., and Haussener, S., 2022, "Multi-configuration evaluation of a megajoule-scale high-temperature latent thermal energy storage test-bed," *Applied Thermal Engineering*, **214**, 9, p. 118697.
- [6] Rezaei, E., Barbato, M., and Gianella, S., 2019, "Pressure drop and convective heat transfer in different SiSiC structures fabricated by indirect additive manufacturing," *J of Heat Transfer-Transactions of the ASME*, **12**, pp. 1–51.
- [7] Agyenim, F., Hewitt, N., Eames, P., and Smyth, M., 2010, A review of materials, heat transfer and phase change problem formulation for latent heat thermal energy storage systems (LHTESS), 2.
- [8] Ibrahim, N. I., Al-Sulaiman, F. A., Rahman, S., Yilbas, B. S., and Sahin, A. Z., 2017, "Heat transfer enhancement of phase change materials for thermal energy storage applications: A critical review," *Renewable and Sustainable Energy Reviews*, **74**, 7, pp. 26–50.
- [9] Liu, L., Su, D., Tang, Y., and Fang, G., 2016, Thermal conductivity enhancement of phase change materials for thermal energy storage: A review, 1.
- [10] Mahdi, J. M., Lohrasbi, S., and Nsofor, E. C., 2019, "Hybrid heat transfer enhancement for latent-heat thermal energy storage systems: A review," *International Journal of Heat and Mass Transfer*, **137**, 7, pp. 630–649.
- [11] Xiao, X., Zhang, P., and Li, M., 2014, "Effective thermal conductivity of open-cell metal foams impregnated with pure paraffin for latent heat storage," *International Journal of Thermal Sciences*, **81**(1), 7, pp. 94–105.
- [12] Yang, J., Yang, L., Xu, C., and Du, X., 2016, "Experimental study on enhancement of thermal energy storage with phase-change material," *Applied Energy*, **169**, 5, pp. 164–176.
- [13] Zhang, P., Meng, Z. N., Zhu, H., Wang, Y. L., and Peng, S. P., 2017, "Melting heat transfer characteristics of a composite phase change material fabricated by paraffin and metal foam," *Applied Energy*, **185**, 1, pp. 1971–1983.
- [14] Gaedtke, M., Abishek, S., Mead-Hunter, R., King, A. J., Mullins, B. J., Nirschl, H., and Krause, M. J., 2020, "Total enthalpy-based lattice Boltzmann simulations of melting in paraffin/metal foam composite phase change materials," *International Journal of Heat and Mass Transfer*, **155**, 7, p. 119870.
- [15] Siahpush, A., O'Brien, J., and Crepeau, J., 2008, "Phase change heat transfer enhancement using copper porous foam," *J of Heat Transfer-Transactions of the ASME*, **130**(8), 8.
- [16] Odabae, M., Hooman, K., and Gurgenci, H., 2011, "Metal Foam Heat Exchangers for Heat Transfer Augmentation from a Cylinder in Cross-Flow," *Transport in Porous Media*, **86**(3), 10, pp. 911–923.
- [17] Chen, K., Guo, L., Xie, X., and Liu, W., 2018, "Experimental investigation on enhanced thermal performance of staggered tube bundles wrapped with metallic foam," *International Journal of Heat and Mass Transfer*, **122**, 7, pp. 459–468.
- [18] Atal, A., Wang, Y., Harsha, M., and Sengupta, S., 2016, "Effect of porosity of conducting matrix on a phase change energy storage device," *International Journal of Heat and Mass Transfer*, **93**, 2, pp. 9–16.
- [19] Wang, C., Lin, T., Li, N., and Zheng, H., 2016, "Heat transfer enhancement of phase change composite material: Copper foam/paraffin," *Renewable Energy*, **96**, 10, pp. 960–965.
- [20] Yang, X., Feng, S., Zhang, Q., Chai, Y., Jin, L., and Lu, T. J., 2017, "The role of porous metal foam on the unidirectional solidification of saturating fluid for cold storage," *Applied Energy*, **194**, 5, pp. 508–521.
- [21] Abishek, S., King, A. J., Nadim, N., and Mullins, B. J., 2018, "Effect of microstructure on melting in metal-foam/paraffin composite phase change

- materials,” *International Journal of Heat and Mass Transfer*, **127**, 12, pp. 135–144.
- [22] Dinesh, B. V. S., and Bhattacharya, A., 2019, “Effect of foam geometry on heat absorption characteristics of PCM-metal foam composite thermal energy storage systems,” *International Journal of Heat and Mass Transfer*, **134**, 5, pp. 866–883.
- [23] Rezaei, E., Barbato, M., Ortona, A., and Haussener, S., 2020, “Design and optimization of a high-temperature latent heat storage unit,” *Applied Energy*, **261**, 3, p. 114330.
- [24] Kollep, M., Konstantinou, G., Madrid-Wolff, J., Boniface, A., Hagelüken, L., Sasikumar, P. V. W., Blugan, G., Delrot, P., Loterie, D., Brugger, J., and Moser, C., 2022, “Tomographic Volumetric Additive Manufacturing of Silicon Oxycarbide Ceramics,” *Advanced Engineering Materials*, p. 2101345.
- [25] Buchanan, C., and Gardner, L., 2019, “Metal 3D printing in construction: A review of methods, research, applications, opportunities and challenges,” *Engineering Structures*, **180**, 2, pp. 332–348.
- [26] Xu, Y., Ren, Q., Zheng, Z. J., and He, Y. L., 2017, “Evaluation and optimization of melting performance for a latent heat thermal energy storage unit partially filled with porous media,” *Applied Energy*, **193**, 5, pp. 84–95.
- [27] Levin, P. P., Shitzer, A., and Hetsroni, G., 2013, “Numerical optimization of a PCM-based heat sink with internal fins,” *International Journal of Heat and Mass Transfer*, **61**(1), 6, pp. 638–645.
- [28] Hilbert, R., Janiga, G., Baron, R., and Thévenin, D., 2006, “Multi-objective shape optimization of a heat exchanger using parallel genetic algorithms,” *International Journal of Heat and Mass Transfer*, **49**(15–16), pp. 2567–2577.
- [29] Akolkar, A., and Petrasch, J., 2011, “Tomography based pore-level optimization of radiative transfer in porous media,” *International Journal of Heat and Mass Transfer*, **54**(23–24), 11, pp. 4775–4783.
- [30] Bendsøe, M. P., and Sigmund, O., 2003, *Topology Optimization - Theory, Methods, and Applications* Springer.
- [31] Alexandersen, J., Aage, N., Andreasen, C. S., and Sigmund, O., 2014, “Topology optimisation for natural convection problems,” *International Journal for Numerical Methods in Fluids*, **76**(10), 12, pp. 699–721.
- [32] Dede, E. M., Joshi, S. N., and Zhou, F., 2015, “Topology optimization, additive layer manufacturing, and experimental testing of an air-cooled heat sink,” In ASME 2015 International Technical Conference and Exhibition on Packaging and Integration of Electronic and Photonic Microsystems, InterPACK 2015, Vol. 3, American Society of Mechanical Engineers (ASME).
- [33] Kaya, M., and Hajimirza, S., 2021, “Nonparametric design of nanoparticles with maximum scattering using evolutionary topology optimization,” *International Journal of Heat and Mass Transfer*, **166**, 2, p. 120738.
- [34] Pizzolato, A., Sharma, A., Maute, K., Sciacovelli, A., and Verda, V., 2017, “Topology optimization for heat transfer enhancement in Latent Heat Thermal Energy Storage,” *International Journal of Heat and Mass Transfer*, **113**, pp. 875–888.
- [35] Pizzolato, A., Sharma, A., Maute, K., Sciacovelli, A., and Verda, V., 2017, “Design of effective fins for fast PCM melting and solidification in shell-and-tube latent heat thermal energy storage through topology optimization,” *Applied Energy*, **208**, 12, pp. 210–227.
- [36] Yao, Q. Y., Zhao, C. Y., Zhao, Y., Wang, H., and Li, W., 2021, “Topology optimization for heat transfer enhancement in latent heat storage,” *International Journal of Thermal Sciences*, **159**, 1, p. 106578.
- [37] Augspurger, M., Choi, K. K., and Udaykumar, H. S., 2018, “Optimizing fin design for a PCM-based thermal storage device using dynamic Kriging,” *International Journal of Heat and Mass Transfer*, **121**, 6, pp. 290–308.
- [38] Dammak, K., and El Hami, A., 2021, “Thermal reliability-based design optimization using Kriging model of PCM based pin fin heat sink,” *International Journal of Heat and Mass Transfer*, **166**, 2, p. 120745.
- [39] Ling, J., and Templeton, J., 2015, “Evaluation of machine learning algorithms for prediction of regions of high Reynolds averaged Navier Stokes uncertainty,” *Physics of Fluids*, **27**(8), p. 85103.
- [40] Tompson, J., Schlachter, K., Sprechmann, P., and Perlin, K., 2016, “Accelerating Eulerian Fluid Simulation With Convolutional Networks,” <https://arxiv.org/abs/1607.03597>, 7.
- [41] Raissi, M., Perdikaris, P., and Karniadakis, G. E., 2019, “Physics-informed neural networks: A deep learning framework for solving forward and inverse problems involving nonlinear partial differential equations,” *Journal of Computational Physics*, **378**, 2, pp. 686–707.
- [42] Lucor, D., Agrawal, A., and Sergent, A., 2021, “Physics-aware deep neural networks for surrogate modeling of turbulent natural convection,”
- [43] Wang, T., Huang, Z., Sun, Z., and Xi, G., 2021, “Reconstruction of natural convection within an enclosure using deep neural network,” *International Journal of Heat and Mass Transfer*, **164**, 1, p. 120626.
- [44] Cai, S., Wang, Z., Wang, S., Perdikaris, P., and Karniadakis, G. E., 2021, “Physics-informed neural networks for heat transfer problems,” *J of Heat Transfer-Transactions of the ASME*, **143**(6), 6.
- [45] Kim, J., and Lee, C., 2020, “Prediction of turbulent heat transfer using convolutional neural networks,” *Journal of Fluid Mechanics*, **882**, 1.
- [46] Guo, X., Li, W., and Iorio, F., 2016, “Convolutional Neural Networks for Steady Flow Approximation,” In Proceedings of the 22nd ACM SIGKDD International Conference on Knowledge Discovery and Data Mining - KDD '16, ACM Press, pp. 481–490.
- [47] Chan, H., Cherukara, M., Loeffler, T. D., Narayanan, B., and Sankaranarayanan, S. K., 2020, “Machine learning enabled autonomous microstructural characterization in 3D samples,” *npj Computational Materials*, **6**(1), 12, pp. 1–9.
- [48] Rabbani, A., Babaei, M., Shams, R., Wang, Y. D., and Chung, T., 2020, “DeepPore: A deep learning workflow for rapid and comprehensive characterization of porous materials,” *Advances in Water Resources*, **146**, 12, p. 103787.
- [49] Van Der Linden, J. H., Narsilio, G. A., and Tordesillas, A., 2016, “Machine learning framework for analysis of transport through complex networks in porous, granular media: A focus on permeability,” *Physical Review E*, **94**(2), 8, p. 022904.
- [50] Tembely, M., AlSumaiti, A. M., and Alameri, W., 2020, “A deep learning perspective on predicting permeability in porous media from network modeling to direct simulation,” *Computational Geosciences*, **24**(4), 8, pp. 1541–1556.
- [51] Tian, J. W., Qi, C., Peng, K., Sun, Y., and Mundher Yaseen, Z., 2022, “Improved Permeability Prediction of Porous Media by Feature Selection and Machine Learning Methods Comparison,” *Journal of Computing in Civil Engineering*, **36**(2), 12, p. 04021040.
- [52] Röding, M., Ma, Z., and Torquato, S., 2020, “Predicting permeability via statistical learning on higher-order microstructural information,” *Scientific Reports*, **10**(1), 12.
- [53] Kamrava, S., Tahmasebi, P., and Sahimi, M., 2020, “Linking Morphology of Porous Media to Their Macroscopic Permeability by Deep Learning,” *Transport in Porous Media*, **131**(2), 1, pp. 427–448.
- [54] Dai, X., 2021, “Numerical characterization and engineering of transport in morphologically complex heterogeneous media,” PhD thesis, EPFL.
- [55] Hajimirza, S., and Sharadga, H., 2021, “Learning thermal radiative properties of porous media from engineered geometric features,” *International Journal of Heat and Mass Transfer*, **179**, 11, p. 121668.
- [56] Kang, H. H., Kaya, M., and Hajimirza, S., 2019, “A data driven artificial neural network model for predicting radiative properties of metallic packed beds,” *Journal of Quantitative Spectroscopy and Radiative Transfer*, **226**, 3, pp. 66–72.
- [57] Santos, J. E., Xu, D., Jo, H., Landry, C. J., Prodanović, M., and Pyrcz, M. J., 2020, “PoreFlow-Net: A 3D convolutional neural network to predict fluid flow through porous media,” *Advances in Water Resources*, **138**, 4, p. 103539.
- [58] Baqué, P., Remelli, E., Fleuret, F., and Fua, P., 2018, “Geodesic Convolutional Shape Optimization,” <https://arxiv.org/abs/1802.04016>, 2.
- [59] Schindelin, J., Arganda-Carreras, I., Frise, E., Kaynig, V., Longair, M., Pietzsch, T., Preibisch, S., Rueden, C., Saalfeld, S., Schmid, B., Tinevez, J. Y., White, D. J., Hartenstein, V., Eliceiri, K., Tomancak, P., and Cardona, A., 2012, Fiji: An open-source platform for biological-image analysis, 6.
- [60] Blender Online Community *Blender - a 3D modelling and rendering package* Blender Foundation, Blender Institute, Amsterdam.
- [61] Weller, H. G., Tabor, G., Jasak, H., and Fureby, C., 1998, “A tensorial approach to computational continuum mechanics using object-oriented techniques,” *Computers in Physics*, **12**(6), 12, p. 620.
- [62] Wolff, F., and Viskanta, R., 1987, “Melting of a pure metal from a vertical wall,” *Experimental Heat Transfer*, **1**(1), pp. 17–30.
- [63] Poirier, D., and Salcedean, M., 1988, “On Numerical Methods Used in Mathematical Modeling of Phase Change in Liquid Metals,” *J of Heat*

- Transfer-Transactions of the ASME*, **110**(3), pp. 562–570.
- [64] Birchenall, C. E., and Riechman, A. F., 1980, “Heat storage in eutectic alloys,” *Metallurgical Transactions A*, **11**(8), pp. 1415–1420.
- [65] Dietrich, B., 2013, “Heat transfer coefficients for solid ceramic sponges- Experimental results and correlation,” *International Journal of Heat and Mass Transfer*, **61**(1), 6, pp. 627–637.
- [66] Sparrow, E. M., and Loeffler, A. L., 1959, “Longitudinal laminar flow between cylinders arranged in regular array,” *AIChE Journal*, **5**(3), 9, pp. 325–330.
- [67] Kyan, C. P., Wasan, D. T., Kintner, R. C., and Wasan, D. T., 1970, “Flow of Single-Phase Fluids through Fibrous Beds,” *Industrial and Engineering Chemistry Fundamentals*, **9**(4), pp. 596–603.
- [68] Kaviani, M., 1995, *Principles of Heat Transfer in Porous Media*, Vol. 53 of *Mechanical Engineering Series* Springer New York, New York, NY.
- [69] Haussener, S., 2010, “Tomography-based determination of effective heat and mass transport properties of complex multi-phase media,” PhD thesis.
- [70] Ma, Z., and Torquato, S., 2018, “Precise algorithms to compute surface correlation functions of two-phase heterogeneous media and their applications,” *Physical Review E*, **98**(1), 7.
- [71] Caruana, R., 1997, “Multitask Learning,” *Machine Learning*, **28**(1), pp. 41–75.
- [72] Rifai, S., Bengio, Y., Courville, A., Vincent, P., and Mirza, M., 2012, “Disentangling factors of variation for facial expression recognition,” In *Lecture Notes in Computer Science (including subseries Lecture Notes in Artificial Intelligence and Lecture Notes in Bioinformatics)*, Vol. 7577 LNCS, Springer, Berlin, Heidelberg, pp. 808–822.
- [73] Ramsundar, B., Kearnes, S., Riley, P., Webster, D., Konerding, D., and Pande, V., 2015, “Massively Multitask Networks for Drug Discovery,”.
- [74] Hassouna, M. S., and Farag, A. A., 2007, “Multistencils fast marching methods: A highly accurate solution to the Eikonal equation on Cartesian domains,” *IEEE Transactions on Pattern Analysis and Machine Intelligence*, **29**(9), 9, pp. 1563–1574.
- [75] Karpathy, A., 2015, “The Unreasonable Effectiveness of Recurrent Neural Networks,” *Web Page*, pp. 1–28.

## 6. Supplementary Information

### 6.1. Macro-Porous Structures Generation

The macro-porous structures are created from 3D stacks of artificially generated tomography data.

#### 6.1.1. Random sub-structures

The tomography data for the random sub-structures can be created as shown in the Fig. S1 which starts with a stack of binary images with randomly assigned pixel values of 0 or 1 (Fig. S1a). 3D Gaussian filters of required kernel sizes (standard deviations) in the three coordinate directions are applied to the binary images to generate the structures depending on the length scale of the porous sub-structures required and the images normalized. The structure of required porosity is then generated using a threshold filter (Fig. S1b).

#### 6.1.2. Ordered sub-structures

The tomography data for the ordered structures are created using a slightly different method. As shown in Fig. S2, a set of points were placed in a cubic arrangement separated by a constant distance and connected by straight lines (both with and without diagonal connections) to obtain a skeletal structure (Fig. S2a). Pixelated spheres of required strut diameters are added along each connecting line in to create 3D image stacks shown in Fig. S2b. Multiple ordered structures as shown in Fig. S3 were created.

#### 6.1.3. STLs from 3D image stacks

The image stacks are process to obtain 3D STLs in the open source 3D image processing package Fiji [59]. Blank 3D stacks of images are added at the top and bottom ends of the generated structures stack to account for the inlet ( $150 \times 150 \times 220$  pixels<sup>3</sup>) and outlet ( $150 \times 150 \times 400$  pixels<sup>3</sup>) lengths. The size of the final 3D image stacks generated including the inlet and outlet is thus  $150 \times 150 \times 1020$  pixels<sup>3</sup>. The following instructions are for the version Fiji ImageJ 1.53f51. The 3D stacks are opened in Fiji by ‘File > Import > Image Sequence’. Gaussian 3D filters are added via ‘Process > Filters > Gaussian Blur 3D’ with sigma of 1 pixel in all directions, so that the final STL surface is smooth. Using ‘Plugins > 3D Viewer’ with the settings for the surface display shown in Fig. S4. The generated STL is exported by ‘File > Export Surfaces > STL (ASCII)’. The open source 3D software Blender [60] was used to remove the physically disconnected regions by going into the ‘Edit Mode’ and ‘Mesh > Clean up > Delete Loose’. The loose parts are removed from the STL to obtain a monolithic surface mesh STL file for the PCM-HTF interface of the macro-porous structure shown in Figs. S1c and S2c.

The 3D STLs were used to create CFD hexahedral meshes shown in Figs. 11d and 12d using the open source meshing code snappyHexMesh in OpenFOAM [61] with multi-layer refinements close to the interfaces.

The CFD mesh generated can be used directly for performing simulations in OpenFOAM or in ANSYS Fluent as shown in this thesis. The mesh is converted to the Enight format using the command `foamToEnightParts` which generates a folder with the name ‘Enight’. The mesh can be imported into ANSYS Fluent by opening the ‘Enight.case’ file in the folder via ‘File > Import > Enight’.

#### 6.1.4. Simulation Settings and Data Processing

The simulation setup was implemented and solved in ANSYS Fluent with the energy, mass, and momentum conservation equations discretized using the second order upwind scheme and time formulation using first order implicit scheme. Pressure-velocity coupling in the continuity equation was discretized using the PIMPLE method with under-relaxation factors (0.85 for pressure, 0.85 for momentum, 0.85 for the melt fraction) and unscaled residuals of  $10^{-6}$  for mass,  $10^{-6}$  for momentum and  $10^{-8}$  for energy. Time and mesh convergence studies were conducted and chosen for convergence and computational efficiency. The phase change simulation for each macro-porous structure had a running time ranging from 9 to 20 hours on 15 CPUs and 40GB RAM depending on the porosity and the complexity of the structure. The GCNN utilized for this work [58] considers the volume and surface meshes of the porous structure along with vertex locations and their connectivity as a tensor input. The tensor form of this input in GCNNs while results in efficient usage of modern tensor based computational hardware, leads to higher memory usage with larger and complicated meshes. This is similar to the scaling problem encountered with 3D CNNs used on binary images. While a hexahedral mesh created using snappyHexMesh with smaller elements closer to the surface to better resolve the flow



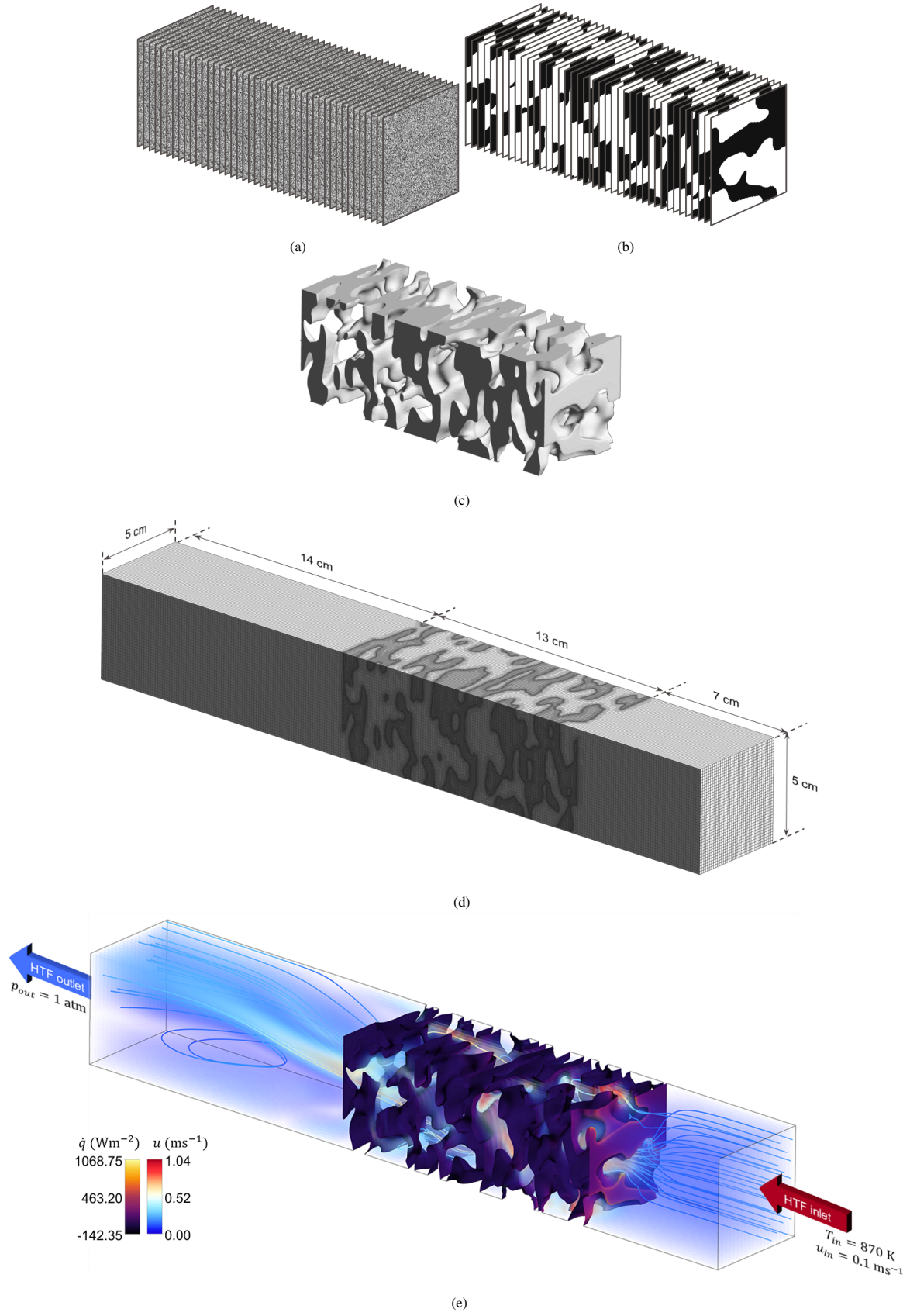


Figure 11: Generation steps of unit-cells of 3D monolithic macro-porous structures with random sub-structure showing (a) 3D image stack with randomly assigned pixels, (b) 3D image stack after applying 3D Gaussian filters and threshold to choose required porosity, (c) STL created from the image stack, (d) CFD compatible hexahedral mesh, and (e) simulation results showing the dimensions, flow direction for the HTF, velocity streamlines and heat flux on the PCM-HTF interface.

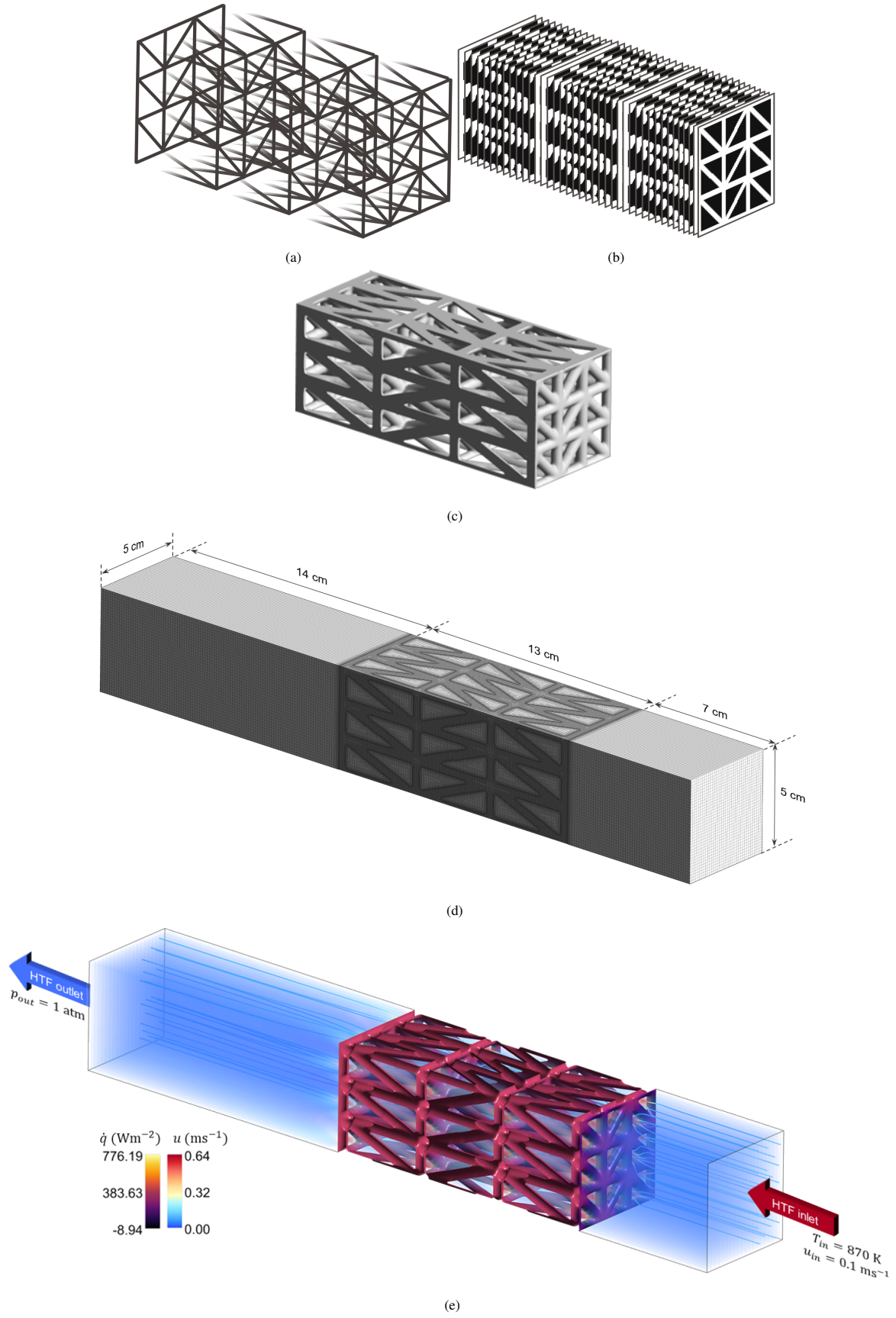


Figure 12: Generation steps of unit-cells of 3D monolithic macro-porous structures with ordered sub-structure showing (a) cubic skeletal structure, (b) conversion to 3D image stack using pixelated spheres traversing the skeleton, (c) STL created from the image stack, (d) CFD compatible hexahedral mesh, and (e) simulation results showing the dimensions, flow direction for the HTF, velocity streamlines and heat flux on the PCM-HTF interface.

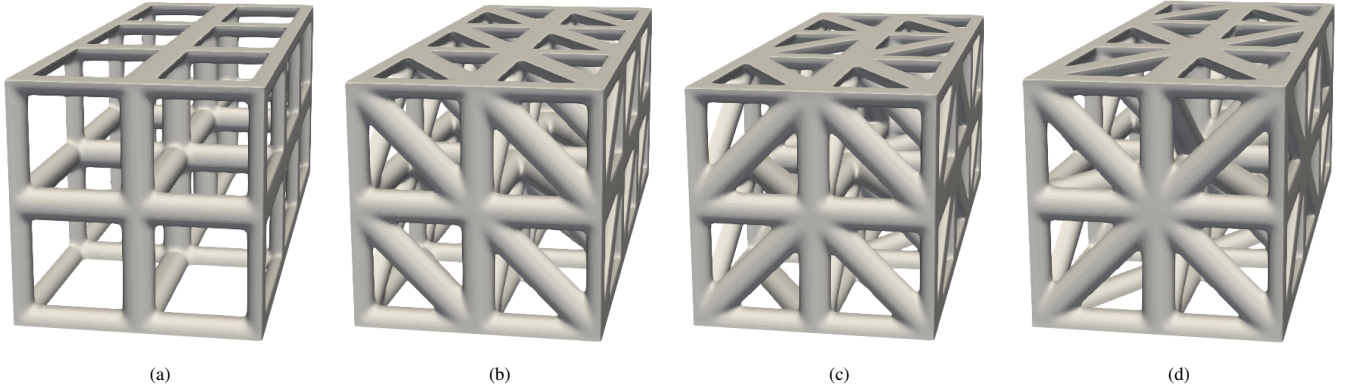


Figure 13: Ordered structures created with the parameters  $\text{cubeSteps} = [2, 2, 3]$ ,  $\text{sphereRad} = 10$ ,  $\text{percRandom} = 0$ , and  $\text{typeLines} =$  (a) 0 for cubic structures, (b) 1 for cubic structures with slashes, (c) 2 for cubic structures with slashes placed in arrow shapes, and (d) 3 for cubic structures with crosses.

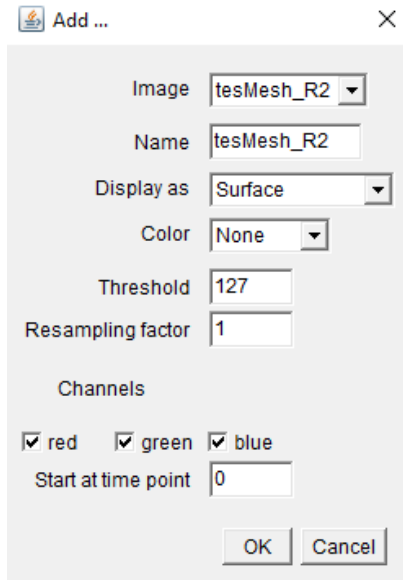


Figure 14: Settings for the '3D Viewer' plugin of Fiji to generate the STLs from the 3D image stacks.

and heat transfer is preferred for simulations, mesh convolution operations run faster with uniform quality, general shape poly-cube mesh. The uniform volume and surface meshes were obtained using interpolation from nearby node values of the original mesh. The surface mesh composed of triangles and quadrilaterals was re-meshed by projecting vertices of a cubic poly-cube mesh onto the original shape of the macro-porous unit-cells [58] before being used as inputs for the GCNN. The simulation results at 10'000 s, when all structures were still in the process of phase change, were exported as temperature,  $T$ , pressure,  $P$ , and velocity,  $u$ , distributions on a volume mesh,  $X_{\text{vol}}$ , of size  $40 \times 40 \times 400$ , and heat flux,  $\dot{q}$ , and shear stress,  $\tau$ , field distributions on a surface mesh,  $X_{\text{surf}}$ , of 70'000 equidistant points, both limited by the memory of the GPU used.

#### 6.1.5. Two-point Correlation Functions

The inputs to the ANN consisted of the macro-porous unit-cell properties, namely  $\phi$ ,  $A$ , and a two-point surface-void cor-

relation functions,  $F_{sv}$ . The correlation function is based on a void indicator function  $\Gamma(x)$  and surface indicator function  $\Pi(x)$  [70] defined as:

$$\Gamma(x) = \begin{cases} 1, & \text{if } x \text{ is in HTF phase} \\ 0, & \text{if } x \text{ is in PCM domain} \end{cases} \quad (5)$$

$$\Pi(x) = |\nabla \Gamma(x)| \quad (6)$$

By this definition,  $\phi = \langle \Gamma(x) \rangle$  and  $A = \langle \Pi(x) \rangle$ , where  $\langle \rangle$  signifies the calculation of the mean value. The two-point surface-void correlation function  $F_{sv}$  at different voxel distances,  $\zeta$ , is given by [70]:

$$F_{sv}(\zeta) = \langle \Pi(x)\Gamma(x + \zeta) \rangle \quad (7)$$

$F_{sv}$  values was calculated for  $\zeta = 1$  to 75 for each structure as the number of pixels in the binary images was 150 in the symmetrical directions of the replicating macro-porous unit-cell.